Masterarbeit

Zur Erlangung des akademischen Grades
Master of Science

Experimental Laboratory Setup for Single-Photon Counting Laser Altimetry in Planetary Research

Eingereicht von:

Stella Meiré

Gutachter:

Prof. Dr. Heinz-Wilhelm Hübers

Prof. Dr. Tim Schröder

Eingereicht am

Institut für Physik

der **Humboldt-Universität zu Berlin** am:

02.10.2023

Zusammenfassung

Laseraltimetrie ist eine Technik zur präzisen topografischen Vermessung planetarer Oberflächen, die tiefere Einblicke in Himmelskörper innerhalb des Sonnensystems ermöglicht. Diese Masterarbeit erforscht das Potenzial der Einzelphotonendetektionstechnologie zur Verbesserung der Laseraltimetrie in der planetaren Forschung. Das Forschungsziel besteht darin, einen selbst entwickelten experimentellen Laboraufbau für die Einzelphotonenzählung in der Laseraltimetrie zu untersuchen, mit dem Ziel, Laserpulse mit der minimal erforderlichen Anzahl von Photonen zu detektieren. Die Studie beginnt mit der Charakterisierung eines Einzelphotonen-Avalanche-Detektors (SPAD), durch die Bestimmung seiner Quanteneffizienz und Dunkelzählrate. Diese Parameter bilden die Grundlage für nachfolgende Experimente. In dieser Arbeit wird die Methode der zeitlichen Filterung eingeführt, bei der ein 80 ns langer Laserpuls verwendet wird, um Laserpulse innerhalb eines kurzen Zeitraums zu detektieren und die Genauigkeit bei der Pulszeitbestimmung zu erhöhen. In dem Laboraufbau wird der Effekt der Einstellungen der Signalübertragung, der Hintergrundstrahlung sowie nachfolgenden Pulsen auf die Erkennung von Laserpulsen untersucht. Die Ergebnisse zeigen eine nichtlineare Beziehung zwischen Signalübertragung, Dunkelzählungen und der Erzeugung von Nachpulsen, die die Genauigkeit bei der Ereigniszählung beeinflusst. Bemrkenswerterweise zeigt der experimentelle Aufbau eine hohe Sensitivität und arbeitet auf Energiestufen, die um Größenordnungen niedriger sind als typische Laseraltimetrie-Instrumente. Diese Forschung liefert Einblicke in das Verhalten und die Leistung von Einzelphotonendetektoren und zeigt deren Potenzial zur Weiterentwicklung der Laseraltimetrie in der planetaren Forschung. Durch die Bewältigung von Störungen, Hintergrundstrahlung und Nachimpuls-Herausforderungen zielt diese Arbeit darauf ab, die Genauigkeit und Empfindlichkeit bei der Vermessung planetarer Oberflächen zu verbessern.

Abstract

Laser altimetry is a technique for precise topographic measurements of planetary surfaces, enabling deeper insights into celestial bodies within the solar system. This master's thesis explores the potential of single-photon detection technology to enhance laser altimetry in planetary research. The research objective is to investigate a constructed experimental laboratory setup for single-photon counting laser altimetry, aiming to detect laser pulses with the minimum required number of photons. The study begins with characterizing a Single Photon Avalanche Detector (SPAD), determining its quantum efficiency and dark count rate. These parameters lay the foundation for subsequent experiments. The research introduces a method called temporal filtering, utilizing an 80 ns laser pulse to detect laser signals within a short timeframe, enhancing precision in pulse timing determination. The impact of transmission settings of the attenuators, background radiation, and afterpulsing on laser pulse detection is investigated. Results show a non-linear relationship between transmission settings, dark counts, and afterpulse generation, affecting event count accuracy. Remarkably, the experimental setup demonstrates a high sensitivity, operating at energy levels orders of magnitude lower than typical laser altimetry instruments. This research provides insights into the behavior and performance of single-photon detectors and demonstrates their potential to advance laser altimetry in planetary research. By addressing noise, background radiation, and afterpulsing challenges, this work aims to contribute to improving accuracy and sensitivity in planetary surface measurements.

Acknowledgments

I extend my sincere appreciation to Prof. Dr. Hübers for his supervision throughout the course of this work.

Furthermore, I would like to thank Prof. Dr. Schröder for agreeing to serve as the second examiner.

I would like to express my gratitude to Dr. Matthias Grott for his oversight and sharing his expertise and guidance.

I am immensely thankful to Jan Binger, who provided me with specific insights in the laboratory.

I am sincerely thankful for the laser altimetry research group at the DLR, including Dr. Matthias Grott, Kay Lingenauber, Christian Althaus, and Jan Binger, for their knowledge and general support.

Inhaltsverzeichnis

Abbildungsverzeichnis

Tabellenverzeichnis

Acronyms

ESA European Space Agency

NASA National Aeronautics and Space Administration

JAXA Japan Aerospace Exploration Agency

DLR Deutsche Zentrum für Luft- und Raumfahrt

J Joule

mJ Millijoule

pJ Picojoule

aJ Attojoule

m Meter

cm Centimeter

km Kilometer

s Second

ms Millisecond

ns Nanosecond

µs Microsecond

1 Introduction

Laser altimetry is a precise technique for measuring topographic features and structures on planetary surfaces using laser pulses[2]. Laser altimeter instruments significantly contribute to planetary research providing accurate distance measurements between a spacecraft and the object of interest. These measurements enable the study and analysis of the surface topography and unique characteristics, leading to a deeper understanding of the diverse bodies within the solar system[13].

Due to their exceptional capabilities, single Photon Avalanche Diodes (SPADs) are important components in laser altimetry[9]. These diodes can detect and precisely time the arrival of individual photons with high temporal resolution, down to a few tens of picoseconds. This unique sensitivity allows laser altimeters to derive time-of-flight information from a single return photon, reducing laser pulse energy and telescope aperture diameter. To further enhance their performance, the adoption of multi-pixel SPAD arrays and detectors with short dead times, combined with statistical evaluation techniques, promises laser altimeters with exceptional precision while conserving resources, making them invaluable tools for planetary research.

The method of laser altimetry centers on measuring the time it takes for light to complete a round-trip journey between the spacecraft and the planetary surface. It is a vital remote sensing method that can be used to create calibrated terrain maps of planetary surfaces, study surface geology and understand celestial body interiors. Detailed analysis of the measurements enables researchers to gain valuable insights into geological processes, surface morphology, and landforms. The data received from other scientific instruments on the spacecraft, such as a camera can be combined with the data of the laser altimeter, which then contribute to mathematical models describing planetary processes and evolution[29].

1.1 Scientific Objectives of Planetary Missions with Laser Altimeter Instruments

The space laser altimeter functions as an active remote sensing device, employing laser technology to analyze and measure the structure of unfamiliar planetary targets. It consists of two essential components: a transmitter and a receiver module.

Inside the transmitter module, a pulsed laser and optical components for transmission enable the emission of laser beams, either as single or multiple shots, with well-defined spatial and temporal patterns. These laser pulses travel through the medium and interact with the ground surface, generating return pulses.

On the receiver side, a telescope, optical components, and a photodetector collaborate to gather and detect the return pulses. The received signals are then transformed into a recognizable format, which can be interpreted by a timing system.

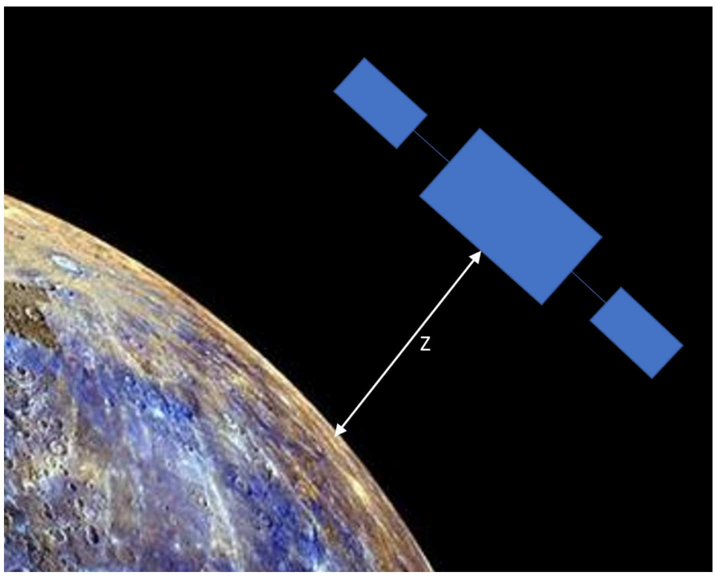

Abbildung 1: **Measurement principle of a laser altimeter.** The parameter z is the distance between the laser altimeter (in blue) and the surface of the planet Mercury to be measured.

A laser altimeter is a specialized tool designed to measure height or distance. It accomplishes this by transmitting laser pulses from the instrument towards the target object's surface. Upon interaction with the object's surface, these pulses reflect and are captured by the instrument's telescope. By measuring the time the laser pulses travel, one can accurately determine the distance to the object's surface.

For each nanosecond (1 ns) of time delay, the laser pulse travels approximately 15 cm in range[36]. The time of flight measurement equation $z = \frac{ct}{2}$, where z represents the distance, c the speed of light and t denotes the time delay, enables accurate measurements of the distance between the instrument and the object's surface. The measurement principle is roughly shown in Fig.1 above. Laser altimeters can generate precise 3D models of the object's surface by continuously measuring distances along the path.

Fig.2 below is a more detailed illustration of the time of flight measurement, which shows the measurement capabilities of a laser altimeter by displaying how an altimeter detector tracks changes in the amplitude of laser pulses over time[2]. The x-axis represents the time and the y-axis represents the optical power. The detector effectively monitors both the laser pulse sent out and the one that is reflected back. The altimeter begins by emitting a laser pulse, the transmitted pulse, which is a burst of laser light that travels toward the target surface. When the laser pulse hits the target surface, it gets scattered and reflected back toward the altimeter, which is called the receiver pulse.

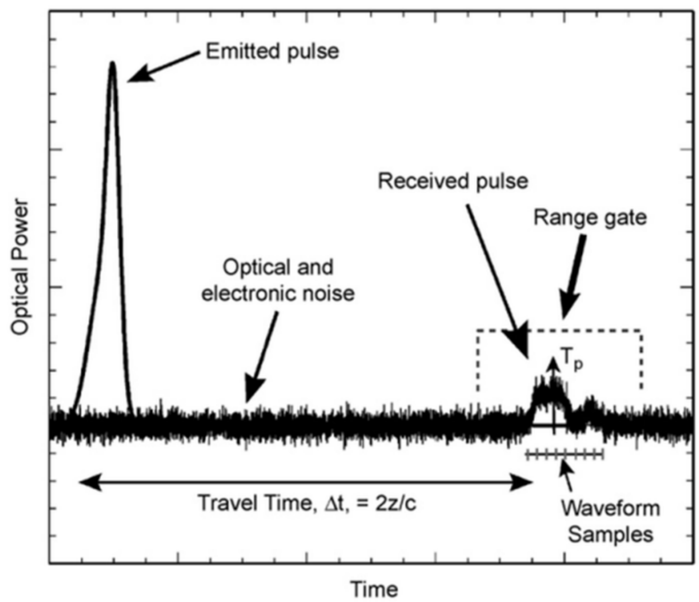

Abbildung 2: **Schematic illustration of the time of flight measurement.** The Illustration portrays how an altimeter detector tracks changes in the amplitude of laser pulses over time, by displaying the optical power of the laser and detector on the y-axis against the time on the x-axis[9].

The received pulse undergoes a transformation when it interacts with the surface. This interaction causes the pulse to spread and distort, a phenomenon that can significantly impact the quality of the data collected. Pulse spreading is more noticeable when dealing with rough surfaces and when measuring through a cloud cover. The distortion directly affects the accuracy of the range measurements.

To precisely measure the time of flight, the altimeter uses a range gate, which is a time window during which the altimeter expects to receive the reflected pulse. The range gate helps in filtering out unwanted signals. Along the base of the received pulse, one can observe a series of regularly spaced marks that indicate the location of waveform digitization samples. These samples are points in time where the intensity of the received pulse is measured, forming a waveform that represents the variation in the pulse intensity over time.

1.2 Classical Laser Altimeters in Planetary Research

In the field of space exploration, laser altimeters have played a crucial role in various missions conducted by space agencies such as ESA, NASA, and JAXA. The following chapters will describe the details of four distinct laser altimeter instruments employed in past missions. This selection includes BELA and GALA, both developed by the ESA in which the DLR played a significant role and ATLAS and LOLA, developed by NASA, each presenting distinctive approaches to laser altimetry.

1.2.1 BepiColombo Laser Altimeter

The BepiColombo Laser Altimeter (BELA) is an instrument on board of the BepiColombo spacecraft which is on a mission to study the planet Mercury [28]. It is a laser altimeter in space within the framework of ESA missions. The mission of BELA is to comprehensively investigate the physical characteristics of Mercury, including its shape, internal structure, and composition.

This involves:

- Analyzing the figure parameters of Mercury to establish precise and reliable reference surfaces;
- Exploring fluctuations in the terrain's characteristics relative to established reference surfaces and constructing a geodetic network by precisely determining the positions of significant topographic features;
- Investigating the deformations in Mercury's surface caused by tidal forces; and
- Evaluating the texture of the surface, gradients in terrain, and changes in reflectivity, with a specific focus on the persistently shaded craters situated near the polar regions.

BepiColombo is a classical laser altimeter equipped with an avalanche photodiode (APD). The measurement principle of the system involves the use of a Nd: YAG laser operating at a pulse energy of 50 mJ, pulse duration of 5 ns and a wavelength of 1064 nm. The laser emits a beam with a spot size ranging from 20 to 50 m. The spot size refers to the diameter of the laser beam and depends on the distance between the spacecraft and the object. BELA is capable of accurately measuring altitudes up to 1050 km above the ground. With a time resolution of 2 ns, the system achieves a height accuracy of approximately 1 m. To put this into perspective, every nanosecond of time resolution corresponds to a distance of approximately 15 cm. This high-resolution capability enables precise measurements and detailed profiling of the surface within the observed region. Fig.3 below shows an illustration of BELA. On the left-hand side, the setup consists of the receiver baffle unit, housing the telescope, while on the right-hand side, the transmitter baffle unit is located, housing the laser. Behind the transmitter baffle unit is the electronic control box. Collectively, these components make up the laser altimeter.

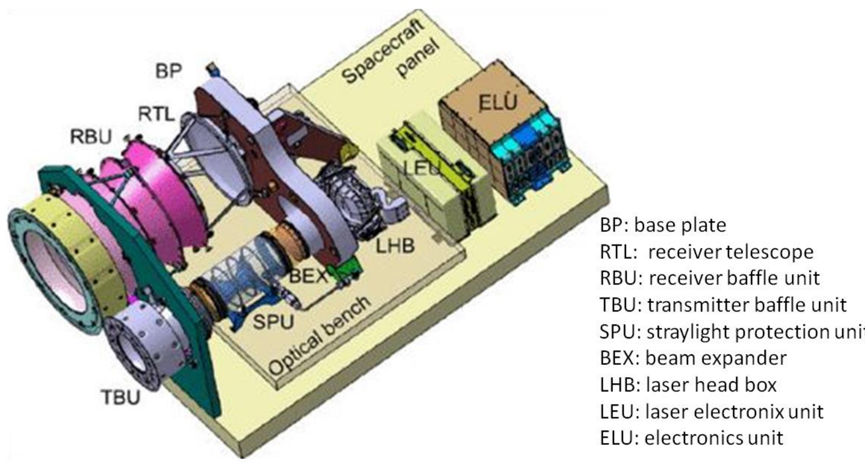

Abbildung 3: **Illustration of the BELA showing the main function units.** These include the telescope, the laser, and the electronic control box[28].

1.2.2 Ganymede Laser Altimeter

The Ganymede Laser Altimeter (GALA) is a remote sensing instrument on the Jupiter Icy Moons Explorer (JUICE)[8]. JUICE launched in 2023 and shall arrive at Jupiter at the end of 2029. One of the objectives of the GALA mission is to acquire topographic data for Jupiter's icy moons, which include Europe, Ganymede, and Callisto.

GALA represents an advanced single-beam laser altimeter. The shot frequency of the laser altimeter lies at 50 Hz and utilizes a wavelength of 1064 nm. The laser pulse of GALA is measured at 5.5 ± 2.5 ns, which means that the duration of the laser pulse generated by GALA typically spans 5.5 ns and the pulse is powered by an Nd: YAG laser. The return pulse is detected using an APD with a bandwidth of 100 MHz. The pulse is digitally sampled at a high rate of 200 MHz, resulting in accurate distance measurements with a detailed subsample resolution down to 0.1 m. This enables detailed mapping and analysis of the surveyed landscapes.

GALA's ability to analyze surface roughness through pulse shape analysis empowers it to extract valuable insights from the pulse return signals, expanding its capacity for surface roughness measurements to cover an area of approximately 50 m from a distance of 500 km.

1.2.3 Lunar Orbiter Laser Altimeter

LOLA stands for Lunar Orbiter Laser Altimeter and is one of the laser altimeter instruments of NASA. LOLA is a scientific instrument installed on NASA's Lunar Reconnaissance Orbiter (LRO)[25]. The purpose of LOLA is to accurately measure the moon's shape by determining the distance between the spacecraft and the lunar surface. Thus, gather data about the moon and expand the knowledge of its structure and surface by creating 3D maps of the moon. The primary objective is to determine the landing site slope and the roughness of the surface. The LRO was launched in 2009 to explore the moon from an orbit around it.

LOLA operates by emitting a brief laser pulse directed towards the lunar surface. This pulse is ingeniously split into five separate beams using a diffractive optical element, and this process occurs at a frequency of 28 Hz. In Fig.4 below, one can observe the footprints of LOLA. The yellow circles represent the laser beams emitted, while the red circles indicate the locations where LOLA has already taken measurements. Upon reaching the lunar surface, the five beams reflect back towards the spacecraft, where five distinct detectors capture them. These detectors allow for the calculation of the distance from the spacecraft to the moon's surface, which is executed at approximately 140 times per second. This primary measurement provides the altimetric distance, which is the distance between the spacecraft and the lunar surface.

Another function of LOLA is assessing pulse spreading, which offers insights into surface roughness. When the laser pulse hits unevenness, such as rocks or irregularities, the pulse, which has the form of a Gaussian curve, undergoes distortion and spreading. Notably, if the surface is even, like water or a sheet of ice, the pulse will not spread. Conversely, when encountering uneven terrain, the pulse returns with observable spreading. While the precise shape of these surface features may remain unknown, LOLA can still provide a rough estimate of the height variations.

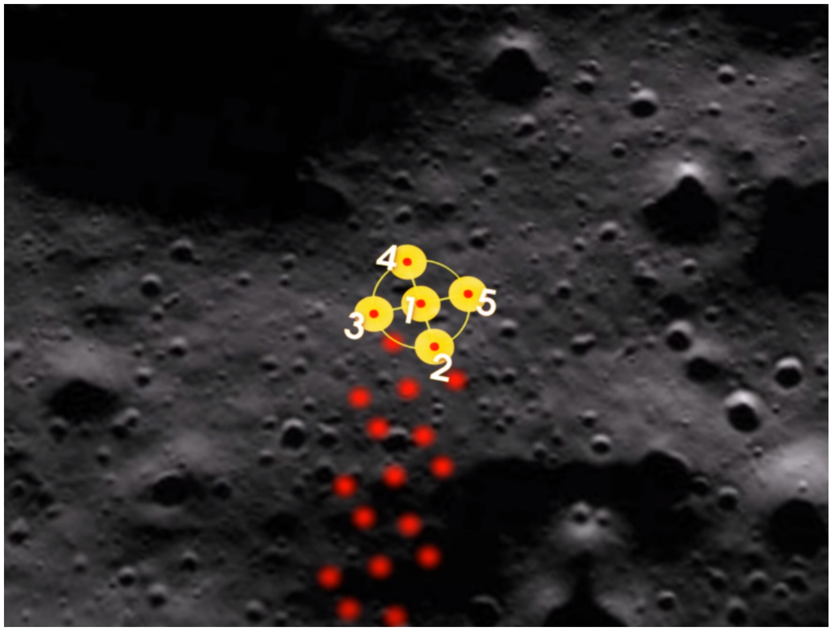

Abbildung 4: **Footprints of LOLA on the moon.** The illustration displays LOLA's projection surface. Yellow circles are laser beams, and red circles are locations where measurements were taken.

1.2.4 Advanced Topographic Laser Altimetry System

The Advanced Topographic Laser Altimetry System (ATLAS) installed on the Ice, Cloud, and Land Elevation Satellite - 2 (ICESat-2) by NASA, launched in 2018, is designed for studying changes in land ice elevation, sea ice clearance above sea level, and for accurately calculating vegetation canopy height globally[14]. Based on the mission of its predecessor, ICESat, ICESat-2 focuses on collecting data for cryospheric research, which pertains to the part of earth's surface containing frozen water. This includes measuring the mass balance of ice sheets and monitoring the thickness and distribution of sea ice. By studying the cryosphere, the aim is to observe changes and trends, enabling the development of climate and future change models.

The laser altimeter utilizes a transmitter that emits a single output beam, which is then partitioned into six beams using a diffractive optical element. Every one of these beams carries approximately one-sixth of the total energy of the laser pulse, which is around 660 mJ. The pulses are extremely short, lasting less than 1.5 ns, and are emitted at 532 nm wavelength. Consequently, the laser beams converge to form a spot on the ground with a diameter of approximately 17 m.

The ATLAS receiver employs a telescope specifically for transmitting green light (532 nm), enabling the collection and concentration of the reflected light of each beam. A combination of pass band coarse filters and optical etalon filters, set to the laser nominal output wavelength, is used to eliminate background light. These filters effectively remove unwanted ambient light and ensure that only the desired signals are received.

1.3 Research Objective

This work aims to introduce a new laser altimeter concept incorporating single photon detection technology, promising to advance altimetry measurements while contributing to resource conservation. This thesis seeks to evaluate an experimental laboratory setup for single photon counting laser altimetry in planetary research, exploring a new approach to single photon detection.

This research is driven by the necessity of a comprehensive investigation and evaluation of the characteristics and parameters of detectors and their implications for various detection schemes. The core objective is to assess how these detector characteristics impact laser altimetry, particularly in the context of planetary research.

To achieve this goal, extensive laboratory experiments to study detector behavior were conducted. A versatile setup was employed with a laser seed driver, an arbitrary pulse generator, and a semiconductor laser diode. This setup allowes the generation of pulses with different shapes, amplitudes, and durations, replicating the conditions encountered in practical altimetry scenarios.

A fiber equipped with electronic variable optical attenuators, bandpass filters, and various optical components transmitted laser pulses to a single-photon counting detector. To simulate typical optical noise, an additional light source was integrated. The primary objective was to leverage a Single Photon Avalanche Detector to precisely locate and reliably detect laser pulses within specific range windows, utilizing the minimum number of photons possible.

1.3.1 Approach

A careful establishment of the laboratory setup is essential for the experimentation process. This involves connecting and assembling all specified laboratory components interfacing them with the required electronics. Initially, an analog photon counter is utilized for preliminary testing and to familiarize with the detector's behavior. Subsequently, the analog photon counter is substituted with a PicoScope due to its superior precision and additional capabilities, enabling the acquisition of electronic timestamped detection counts.

The initial step focuses on characterizing the detector and understanding its performance. This entails measuring the quantum efficiency as a function of gain, which provides fundamental insights into its ability to detect photons emitted by laser pulses. This measurement quantifies the number of detected photons relative to the laser pulses emitted.

Following this, attention is turned to determining the dark count rate, which signifies the count of detections that occur even in the absence of incident light. This parameter is essential for distinguishing between laser pulses or dark events during subsequent measurements.

The subsequent phase is dedicated to the precise detection of the laser signal. Various laser pulses are directed toward the detector, and their characteristics concerning duration are systematically examined through measurements. A method is developed to differentiate the laser signal from other detected events. This comprehensive approach ensures a profound understanding of the detector's performance characteristics, thus enabling precise and reliable measurements in the later stages of the research.

2 Components for Laser Altimeters

2.1 Principles of Lasers

Laserßtands for Light Amplification by Stimulated Emission of Radiation[10][19]. Lasers produce a beam of light based on the principle of stimulated emission of radiation. A laser beam possesses distinct characteristics that distinguish it from other types of light. Specifically, the beam is monochromatic, i.e., it produces only one color. It is coherent, i.e., the waves emitted are all in phase and collimated, which results in a beam with high directionality.

Laser sources are devices that generate intense, coherent beams of light through stimulated emission, with diverse applications in industry, research, and everyday life. There are different types of lasers depending on the materials they use as the active medium, which will be explained in chapter 2.1.2. Solid-state lasers use solid materials (usually doped crystals or glasses), semiconductor lasers use semiconductor materials like gallium arsenide (GaAs), and fiber lasers use optical fibers doped with rare earth ions. Each type of laser has its unique properties and applications.

2.1.1 Spontaneous and Stimulated Emission, Absorption

To explore the various ways energy interactions occur within atomic systems, it is essential to understand three fundamental processes: Spontaneous and stimulated emission and absorption[27]. These processes are central to the behavior of electrons within atoms. In an atom, electrons occupy discrete energy levels. Each energy level corresponds to a specific energy value for the electrons, which can be determined using the following Einstein formula:

$$E_1 - E_2 = \Delta E = h\nu = h\frac{c}{\lambda} \tag{1}$$

The variable E represents the energy in joule, $h = 6.627 \times 10^{-34} \frac{J}{Hz}$ represents the Planck constant, ν the frequency in the unit Hz, $c = 3 \times 10^8 \frac{m}{s}$ is the velocity of light and λ represents the wavelength in meter.

A spontaneous emission, illustrated in Fig.5(a), occurs when considering two energy levels ($E_1 < E_2$), and an electron is initially in level 2. The electron tends to transition to a lower energy level. When this happens, energy is released as an electromagnetic wave or a photon with the energy ΔE, and it is referred to as spontaneous emission. Now considering a scenario where the electron initially resides in E_2, illustrated in Fig.5(b), and an electromagnetic wave with a frequency μ equal to the natural frequency of the electron impinges on the material. When these frequencies match, there is a chance that the incoming wave will induce the electron to make a transition from E_2 to E_1. In this process, the energy difference ΔE is released as an electromagnetic wave, which combines with the incident wave. This phenomenon is known as stimulated emission. When a photon hits an electron in a lower state E_1, for example, the ground state, and has the same energy as the difference ΔE, then the electron absorbs the photon and jumps into a higher state E_2. This process is called absorption and is illustrated in Fig.5(c).

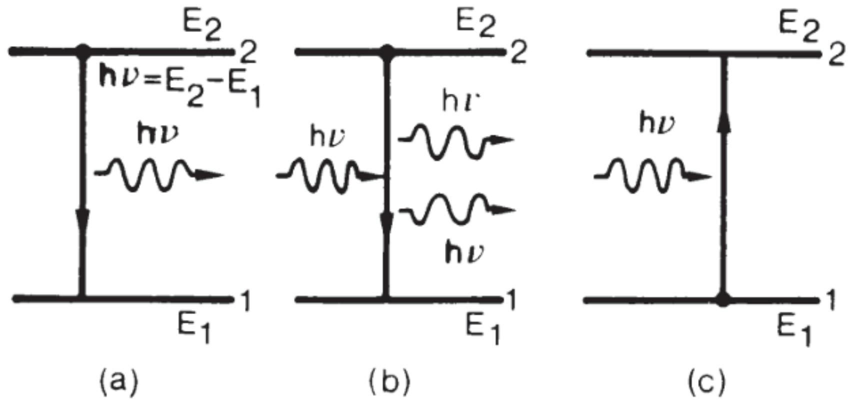

Abbildung 5: **Illustration of the radiative processes.** Including (a) the spontaneous emission, (b) the stimulated emission, and (c) absorption[27].

2.1.2 Laser Construction

Lasers consist of three parts: the active medium, the pump, and the resonator[27]. The pump supplies energy to the system and creates a population inversion in the active medium, which will be described below. The resonator consists of two parallel mirrors and amplifies and aligns the laser beam. The active medium can be solid, gas, or liquid, depending on the type of laser. The optical resonator is an arrangement of mirrors that forms a closed, reflective enclosure for the laser's active medium.

In the active medium, population inversion must be created for stimulated emission to be possible, which is vital for the operation of a laser. Achieving population inversion means having more electrons in the higher energy state (excited state) than in the lower energy state (ground state)[19]. This is essential for laser operation because it sets the stage for stimulated emission, which is the amplification process in lasers. To sustain population inversion, it is essential to have multiple energy states.

One can achieve population inversion by bringing the electrons into an excited state by supplying energy through optical excitation or electrical discharge, known as the pumping process[21]. Once the population inversion is achieved, more atoms are in an excited state than in the ground state. This increases the chance for an excited atom to release another photon because of stimulated emission with the same phase and direction of the incoming photon. This sets off a chain reaction where more and more photons are produced and amplified due to the population inversion. The number of photons grows fast, which leads to a high amount of light within the active medium. This intensified light beam can then exit through a partially reflective mirror, forming the laser beam.

2.1.3 Energy Level Systems

There are two different kinds of laser energy level systems, which play a crucial role in achieving population inversion in the active medium of a laser[21][27]. The first is the three-level laser system shown in Fig.6(a). This process involves pumping the electrons from the lowest energy level (1) to the highest energy level (3). From there, the population can rapidly decay down to the second energy level or back down to the first. The electrons that reach the second energy level become available for stimulated emission. When an electromagnetic wave matches the energy difference between the second and first energy levels, it triggers stimulated emission, producing the laser beam.

The four-level laser systems follow a similar process, but with a slight difference as shown in Fig.6(b). Initially, energy is pumped into the system, raising the electrons from the lowest energy level (0) to the highest energy level (3). Once the electrons are at the highest level, they quickly transition to the second energy level (2). This is called the metastable state, which is essentially a long-lasting energy state that resides at the second energy level and is not the highest in the system. Laser emission occurs when incoming electromagnetic waves match the energy difference between the second energy level (2) and the first energy level (1). When this energy match occurs, it prompts stimulated emission. During this process, photons are emitted in sync with the incoming photons, leading to light amplification. Following the laser emission, the electrons at the second energy level (2) eventually return to the ground level (0).

In both the three-level and the four-level systems, the primary steps involve the excitation of electrons to higher energy levels (achieved through pumping), their subsequent transition to lower energy levels, and finally, the process of stimulated emission. This stimulated emission results in the amplification of light and the generation of the laser beam.

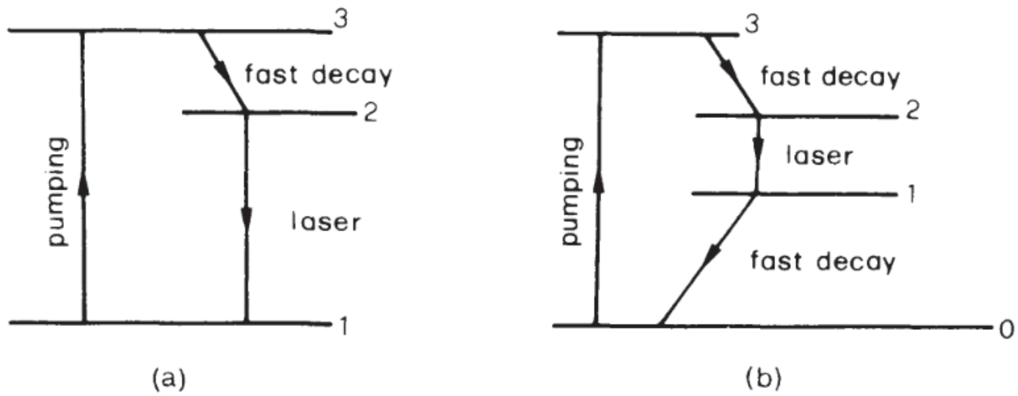

Abbildung 6: **The laser energy level systems for laser light emission.** Demonstrating (a) the three-level system, and (b) the four-level system [27].

2.2 Types of Laser Sources

2.2.1 Continuous Wave and Pulsed Lasers

Continuous wave (CW) lasers and pulsed lasers are two fundamental modes of operation in laser technology, each with distinct characteristics and applications. CW lasers emit continuous, harmonically stable waves with a constant amplitude [10], making them ideal for applications requiring a steady and monochromatic source of electromagnetic radiation. In contrast, pulsed lasers produce high-intensity bursts of light with variable pulse durations[27], making them well-suited for applications where peak power and control over the energy delivery are critical. Pulsed lasers are often employed in fields such as material processing, and laser fusion research, where the ability to achieve extremely high peak powers in short timeframes is essential. On the other hand, CW lasers find widespread use in areas like telecommunications, and scientific research where a continuous and stable output is preferred. The choice between continuous and pulsed lasers depends on the application's specific requirements, with each mode offering unique advantages and capabilities.

2.2.2 Diode Lasers

Diode lasers use a semiconductor diode as the active medium to generate light[27]. These lasers operate on the principle of electroluminescence, where an electric current is passed through a semiconductor material, causing it to emit light. Semiconductor lasers need a specific type of material known as a direct-gap material, which means regular elemental semiconductors like silicon (Si) cannot be utilized. Rather than that, the majority of semiconductor laser materials are crafted using elements found in the third group (such as Aluminum, Gallium, Indium) and the fifth group (including Nitrogen, Phosphorus, Arsenic, Antimony) of the periodic table. These elements combine to create what is commonly known as III-V compounds.

These lasers work by applying a voltage that exceeds a threshold voltage through a semiconductor material, creating a population inversion of electrons and holes at a p-n-junction. A p-n-junction is the interface between two semiconductor regions, one doped with electron-deficient (p-type) material and the other doped with electron-excess (n-type) material. The p-n-junction will further be described in chapter 2.3.1. When the electrons recombine with the holes, photons are emitted in a process known as spontaneous emission. Moreover, the emitted photons stimulate other excited electrons to release more photons through stimulated emission, which further amplifies the light. The emitted photons are then amplified as they reflect back and forth between two mirrors at the end of the diode. This produces a narrow and coherent beam of light that exits the diode as a laser beam.

The extensive utilization of laser diodes can be attributed to their small size and energy efficiency. The ability to control the output power of diode lasers makes them highly adaptable to different applications. Their compact size allows integration into various devices and systems.

2.2.3 Nd:YAG Lasers

An Nd:YAG (neodymium-doped yttrium aluminum garnet) laser is a type of solid-state laser. A solid-state laser uses a solid material, mostly a crystal, as the active medium. In this case, the Neodymium ions (Nd3+) are embedded in the YAG crystal, serving as the active centers. To generate the laser beam, these active centers are placed within the resonator of the laser, which includes mirrors at each end[21]. The mirrors create an optical resonator, allowing light to bounce back and forth, stimulating the emission of coherent photons from the Nd3+ ions. This process amplifies the light, and when it reaches a certain level of intensity, a fraction of it is extracted from the resonator through a partially reflecting mirror, resulting in the laser beam output. Nd:YAG lasers can produce both CW and pulsed light. Instead of electrons which are excited in a semiconductor laser, solid-state lasers are based on ions being excited in the crystal and they operate in a four-level energy system.

To induce the necessary energy levels, the laser employs optical pumping techniques with xenon or krypton flash tubes, which serve as a pumping source. The Nd3+ ions are exited to higher energy states. As these ions transition from a metastable state back to a ground state, they emit a laser beam with a wavelength of 1064 nm.

The Nd:YAG lasers are often used because of their high thermal conductivity, high repetition rate, and low threshold for laser operation and it is easier to achieve population inversion.

2.2.4 Fiber Lasers

Fiber lasers use an optical fiber as the gain medium[24]. The fiber is typically doped with rare earth ions (e.g., ytterbium, erbium) to achieve the necessary gain for laser emission. Fiber lasers are known for their high efficiency, excellent beam quality, and compact size.

Fiber lasers possess several advantages owing to the compact size of their active core. This small core volume contributes to their ability to operate efficiently with a low energy input threshold. Furthermore, their excellent heat dissipation stems from the relatively large surface area of the fiber compared to its interior volume. To create the reflective surfaces at the ends of the fiber, which function equivalent to resonator mirrors, fiber gratings are employed, known as fiber Bragg gratings (FBGs).

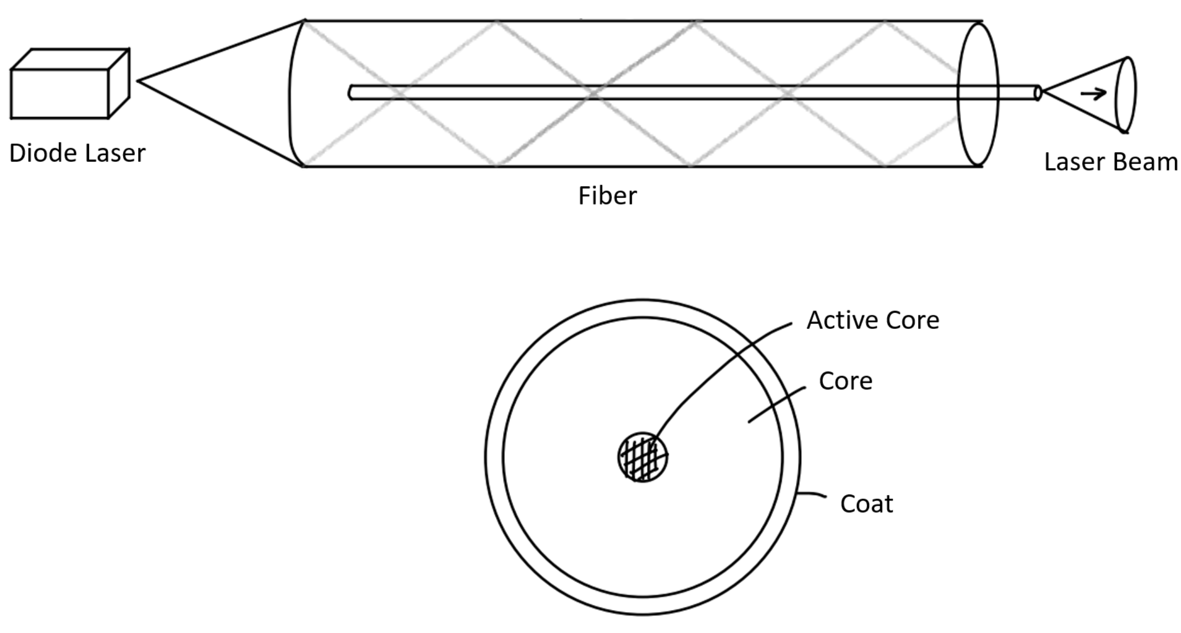

Abbildung 7: **A diode-pumped fiber laser with a dual-core structure.** At the top of the image, the construction of a diode-pumped fiber laser is depicted, while below, is a cross-sectional view of the dual-core.

When it comes to single-mode fiber lasers, they emit a continuous output of power of a few watts. However, significantly higher power levels can be achieved with dual-core fiber lasers. In this setup, the pumping process occurs through a dual-core structure, shown in Fig.7. The active core, typically the size of $5 - 9\,\mu$m in diameter, is enveloped by a second core, known as the pump core, with a diameter ranging from 100 to 400 μm. This arrangement enables pumping throughout the entire length of the fiber, resulting in a power of a few kilowatts. These high power levels are usually limited by nonlinear optical effects, such as stimulated Raman scattering, which becomes more pronounced at higher intensities, or by potential material damage.

2.3 Detectors

In this chapter, various types of detectors will be introduced, along with detailed explanations of their operational principles, functions, and applications.

2.3.1 Photodiodes

A photodiode is a semiconductor device, consisting of a structure with a p-n junction or a p-i-n junction, that converts light into an electric current[11]. It operates on the principle of the photoelectric effect, which is the phenomenon where exposure to light causes the emission of electrons from a material, dislodging them from their atoms and creating an electric current. The working principle of a photodiode is similar to that of a standard p-n junction diode. However, photodiodes often use a p-i-n (p-type, intrinsic, n-type) structure, which includes an intrinsic zone to provide a faster response time.

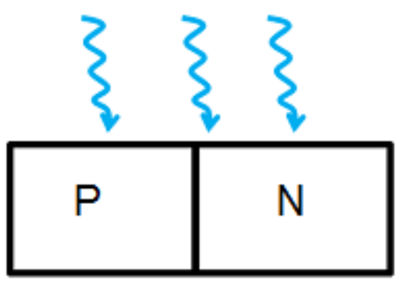

Abbildung 8: **Illustration of a p-n junction photodiode.** The P and N regions are two positively and negatively doped regions. The blue arrows demonstrate incident photons, which are about to strike the p-n junction[18].

A photodiode with a standard p-n junction, which is shown in Fig.8, consists of two regions: a p-type region, which is doped with positive charge carriers, and an n-type region, doped with negative charge carriers. Bringing these two regions together forms a p-n junction. When no external voltage is applied, the free charge carriers in the p and n regions, are in equilibrium. When a reverse voltage (opposite to the direction of normal current flow) is applied to the photodiode, it creates a depletion zone. This depletion zone is an area where there are very few free charge carriers, as they have been pushed away by the electric field caused by the reverse voltage.

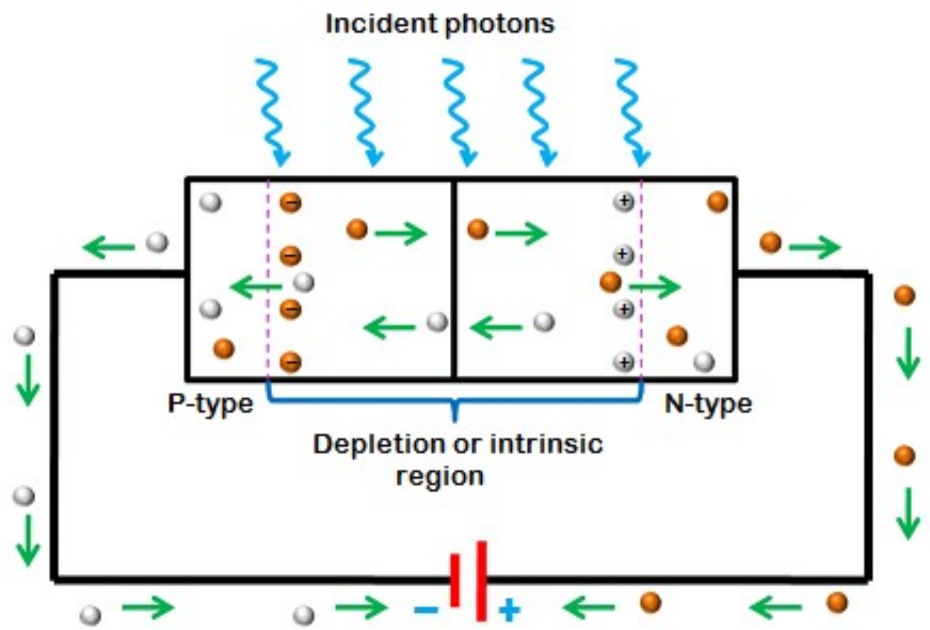

Abbildung 9: **Illustration of the operating principle of a p-n and p-i-n junction photodiode.** The blue arrows represent the incident photons, which strike the depletion or intrinsic region, depending on the structure of the junction, and create mobile electron-hole pairs. The reverse voltage's electric field separates the electron-hole pairs. As indicated by the green arrows, electrons move toward the positive side of the photodiode and holes toward the negative side[18].

When light photons[11], also called incident photons, strike the p-n junction, they create a mobile electron-hole that pairs within the depletion zone. The operation of a photodiode is illustrated in Fig.9. The electric field created by the reverse voltage causes these electron-hole pairs to be separated. The electrons are attracted to the positively charged side of the photodiode, while the holes are attracted to the negatively charged side, represented by the green arrows.

This separation of electron-hole pairs results in a photocurrent, which is proportional to the number of photons absorbed. To measure the photocurrent, the photodiode is typically connected to an external circuit, to convert the current into a voltage that can be measured. The photocurrent and voltage can then be used to determine the intensity of the incident light.

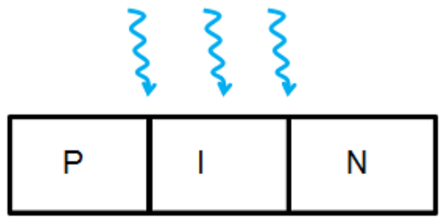

Abbildung 10: **Illustration of a p-i-n junction photodiode.** Same as in Fig.8, but including an additional intrinsic zone, which is an undoped region to enhance sensitivity and response time[18].

A photodiode with a p-i-n structure consists of three regions that are either p-doped or n-doped, which means they have an excess of positive or negative charge carriers, shown in Fig.10. Between these two doped regions is an undoped zone known as the intrinsic zone. In the intrinsic zone, the concentration of free charge carriers is determined by the impurities in the material rather than intentional doping.

The primary difference between a standard p-n junction photodiode and a p-i-n junction photodiode lies in the presence of an additional intrinsic region. In a standard p-n photodiode, light absorption occurs directly in the depletion region, while the intrinsic region extends into the area where light is absorbed. This feature in the pin structure enhances sensitivity and response time, making pin photodiodes preferable to applications requiring high-speed and high-sensitivity light detection.

2.3.2 Avalanche Photodiodes

An avalanche photodiode (APD) is a highly sensitive photodetector that leverages the principle of avalanche multiplication to amplify signals upon photon absorption, utilizing the photoelectric effect[35]. Operating in the avalanche mode, APDs are designed to deliver superior sensitivity and gain, compared to standard photodiodes. The structure of an APD resembles that of a conventional photodiode, featuring a p-i-n junction. However, it includes an additional heavily p-doped layer known as the avalanche region within the depletion zone.

The primary distinction between an avalanche photodiode and a conventional photodiode lies in the internal signal amplification, achieved through the signal's avalanche multiplication. In the layer structure of a conventional photodiode with the p+-i-n+ configuration, a p+ layer, indicating a heavily p-doped layer, and an i-layer, the intrinsic zone, and an n+ layer, indicating a heavily n-doped layer, a p-layer (p+i-p-n+)

is added to the APD, as illustrated in Fig.11. The additional p-layer has the biggest resistance, which leads to the largest electric field value, because of the chosen profile of the distribution of the dopants.

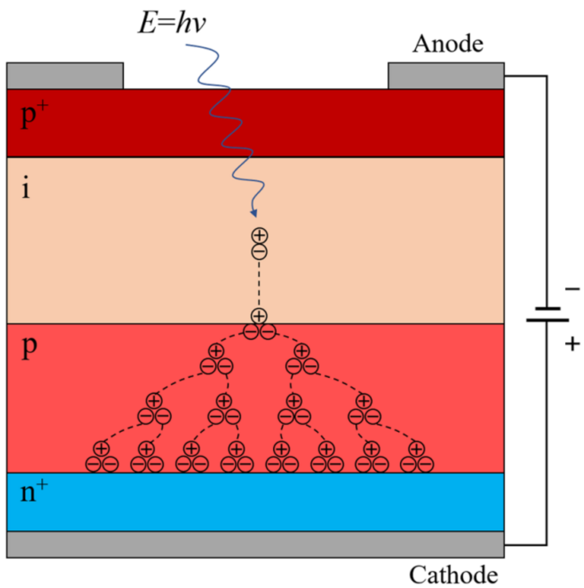

Abbildung 11: **The layer structure of an avalanche photodiode.** A heavily doped p and n layer, an intrinsic zone, and an extra p layer with a strong electric field, cause electrons or holes to gain kinetic energy, leading to impact ionization and the generation of more electron-hole pairs through successive collisions[35].

To trigger the avalanche process, a high reverse bias voltage is applied to the APD, represented by the anode and cathode in the illustration, generating a robust electric field across the avalanche region [11]. When a photon with sufficient energy is absorbed in the avalanche region, it generates an electron-hole pair, similar to a regular photodiode. However, due to the intense electric field, the electron or hole acquires enough kinetic energy to impact other atoms in the avalanche region. This impact ionization initiates the creation of additional electron-hole pairs through successive collision. Each new pair further gains energy and participates in the creation of more pairs, leading to an avalanche multiplication effect. This results in a substantial increase in the number of electron-hole pairs, leading to a significant boost in current gain.

The amplification of signals in APDs allows them to achieve signal detection even with a relatively low number of incident photons. This makes them highly advantageous for applications requiring enhanced sensitivity in detecting weak light signals.

2.3.3 Photomultipliers

A photomultiplier is a detector capable of registering individual photons by using the photoelectric effect [11]. A single electron, which is typically produced by the photoelectric effect when a photon strikes a surface, is too weak to register as a measurable electrical current or signal. To overcome this limitation, photomultiplier tubes (PMTs) are employed. PMTs are devices designed to amplify the number of electrons produced through the interaction of photons with a photosensitive surface. This amplification process is achieved through multiple dynode stages within the photomultiplier tube.

Shown in Fig.12, a photomultiplier consists of three parts: a photocathode, a series of dynodes, and an anode. A vacuum is maintained within the tube. When light enters the tube through a window and strikes the photocathode, it can release an electron, but only if the energy of the incoming light exceeds the threshold. This threshold corresponds to the binding energy of the material, which must be surpassed by the energy of the incoming photon for electron emission to occur. Individual photoelectrons are released within the tube's vacuum and directed towards the first dynode by an electric field created by a high voltage. At the first dynode, these electrons undergo a multiplication process facilitated by the emission of secondary electrons. This sequential process repeats itself at each subsequent dynode until the secondary electrons from the last dynode are gathered at the anode. A single photoelectron undergoes significant amplification through this mechanism, reaching a multiplication factor ranging from 10^5 to 10^7. The resulting amplified signal can then be further processed as an electrical signal.

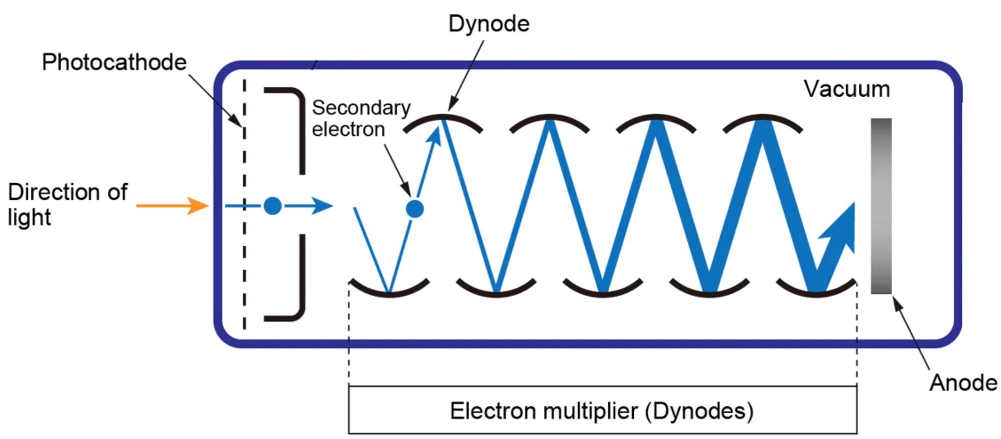

Abbildung 12: **The structure of a photomultiplier tube.** The photomultiplier tube consists of a photocathode, dynodes, and an anode. Incoming light triggers electron release if it exceeds the material's binding energy. The electrons are then multiplied at the dynodes and culminate at the anode.

2.3.4 Single Photon Avalanche Diodes (SPADs)

Single Photon Avalanche Diodes (SPADs) are specialized photodiodes operating in the so-called Geiger mode above the breakdown voltage[3]. These devices are designed to detect and register individual photons with exceptional sensitivity. When a single photon impacts the SPAD, it initiates the generation of an electrical signal, enabling efficient photon detection. Due to their unique operating mode, SPADs are biased slightly above the breakdown voltage, known as the avalanche voltage, and are operated by applying a reverse bias voltage. This means applying a voltage with the opposite polarity to that of the intrinsic voltage direction of the semiconductor material, typically applying a negative voltage to the anode and a positive voltage to the cathode.

This configuration has a specific dead time, during which no further photon detections can occur because the device is in a saturated state. The use of avalanche-quenching circuits is crucial for SPADs to effectively detect individual photons without damaging the diode. These circuits are designed to limit the avalanche effect in the SPAD after detecting a photon and ensure that the diode is not permanently damaged. The principle of SPADs will be described more in detail in Ch.3.

Compared to APDs, SPADs exhibit significantly higher sensitivity, as evidenced by their capability to generate a signal from only a single photoelectron. This enhanced sensitivity makes SPADs particularly well-suited for applications that require the detection of extremely low levels of light. Moreover, the unique characteristics of SPADs have made them a preferred choice in applications aiming to conserve energy and reduce mass. The ultimate goal is to miniaturize setups while maintaining high-performance photon detection capabilities.

3 Physics of SPAD Detectors

3.1 Operation in Geiger Mode

The Single Photon Avalanche Diode operates in the Geiger mode, which requires a higher voltage compared to regular operations [33][3]. The operating principle is illustrated in Fig.13. In Geiger mode, the diode is operated with a reverse bias, which means a voltage is applied in the opposite direction to its usual direction. This voltage is called the avalanche voltage V_{A} and is set just above a specific threshold voltage called the breakdown voltage V_{BD}, which is explained in more detail in Ch. 3.1.1. By operating the diode just above the breakdown voltage, the SPAD becomes highly sensitive to incoming photons. Until a photon arrives, the SPAD stays in a metastable state, called the Geiger mode.

The SPAD then functions as follows: When a photon strikes the SPAD, it starts a process of ionization within the diode through the photoelectric effect. The ionization process generates pairs of electrons and holes. Due to the applied higher voltage, the electron within the SPAD triggers an avalanche multiplication, leading to a significant number of electrons and holes (Pt.1 to Pt.2). As a result, an observable flow of current, resembling an avalanche of electrons, is generated (Pt.2). An active quenching circuit is then needed to reduce the current and the bias voltage below the breakdown voltage(Pt.3). Finally the detector recovers and regains to the avalanche voltage (Pt.3 to Pt.1).

3.1.1 Breakdown Voltage

The breakdown voltage also referred to as the excess bias voltage, holds significant importance in the photon counting process[3]. The breakdown voltage is the minimum voltage at which a semiconductor material, such as a diode, experiences a rapid increase in conductivity and allows the flow of electrical current. It is the voltage level at which the diode begins to break down and conduct electricity in the reverse-biased direction. In an SPAD operating in Geiger mode, the detector remains in a metastable state, indicating that it is biased beyond the breakdown voltage. This metastable state indicates the condition where the detector is awaiting the arrival of a photon. An intense electric field is established by biasing the detector slightly above the breakdown voltage, enabling the detection of even a single photon that enters the intrinsic zone in the p-i-n junction, triggering an avalanche.

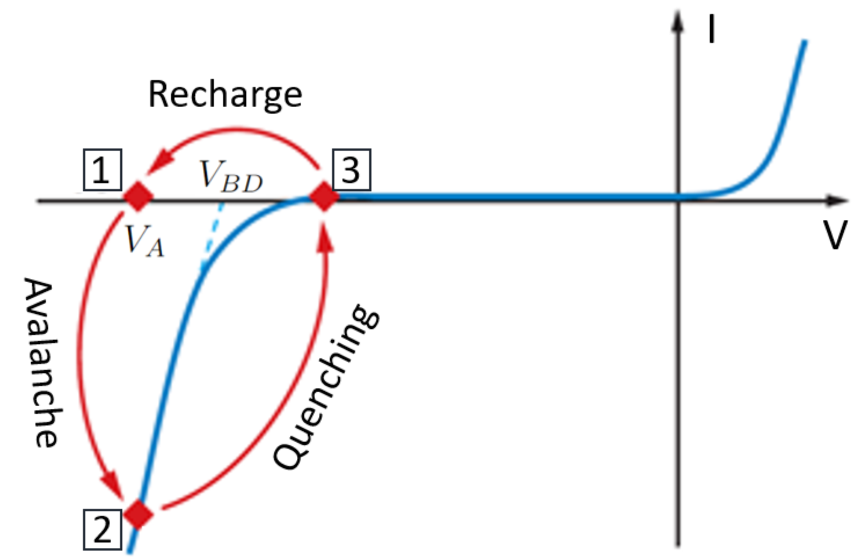

Abbildung 13: **SPAD operating in Geiger mode.** The diagram depicts a current-voltage diagram, with current on the y-axis and voltage on the x-axis. The SPAD is in Geiger mode at the avalanche voltage, residing in a metastable state until a photon arrives. When a photon triggers ionization, it leads to electron-hole pairs and an avalanche multiplication (1 to 2). An active quenching circuit then reduces the current and the bias voltage (3).

3.1.2 Dead Time

The recovery time of an SPAD refers to the time when the SPAD is not able to detect any new incoming photons[33]. It is also known as the quenching time or the dead time of a detector[3]. It is the time for the detector to recharge. The dead time depends on whether the diode is being quenched actively or passively.

3.1.3 Active and Passive Quenching

Active quenching circuits are designed to prevent the destruction of the device by limiting the current and rapidly reducing the bias voltage below the breakdown voltage immediately after an avalanche is triggered by a photon[3]. This functionality allows for high count rates while leading to a dead time between individual counts.

SPADs can employ both active and passive quenching circuits. Active quenching systems provide precise control over the duration of the dead time, in contrast, passive quenching systems may result in inconsistencies in photon counting. These inconsistencies can arise due to variations in the magnitude of electrical signals (known as peaks) generated when a photon is detected and due to irregularities in the duration of the dead time.

In the design of the detector, an active quenching system is used to regulate the dead time and to improve the consistency of the duration of the dead time. The active quenching system works as follows, illustrated in Fig.14:

- The rapid increase in voltage V_{A} above the threshold voltage V_{BD} during the avalanche pulse is detected by a high-speed comparator - The Reset Transition.
- When the comparator detects the voltage rise, it immediately adjusts the bias voltage source to a value equal to or below the breakdown voltage V_{BD}. This effectively stops the avalanche process - The Quenching Transition.
- Following a precisely controlled period of time, referred to as the hold-off time, the bias voltage is reverted to its standard operating level V_{A}.
- Additionally, the comparator generates a consistent pulse that aligns with the rise of the avalanche pulse. This pulse is useful for tasks such as counting photons and accurately timing events.

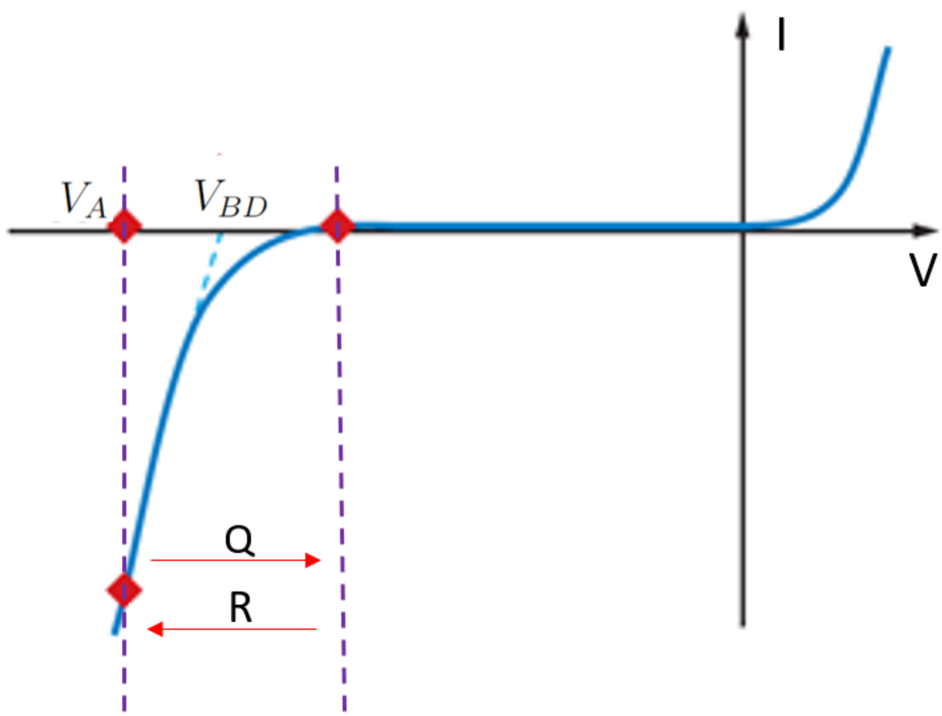

Abbildung 14: **An illustration of an active quenching system.** The diagram depicts a current-voltage diagram, with current on the y-axis and voltage on the x-axis. Q displays the quenching transition of an SPAD in Geiger mode and R displays the reset transition.

3.1.4 Gain Adjustment

To maximize the performance of SPADs in Geiger mode, continuous adjustments are crucial for optimizing the output signal[33] [12]. One of the main factors in achieving this optimization is the ability to control the bias voltage applied to the detector. The bias voltage refers to the specific voltage applied to the SPAD, influencing its avalanche breakdown behavior. Increasing the voltage leads to a higher gain, thereby increasing the photon detection efficiency. In Fig.13, as the gain increases, the avalanche voltage V_{A} rises, causing it to shift further to the left on the graph. This leftward shift indicates an upward trend in the relationship between gain and avalanche voltage. This means that the detector can detect a higher percentage of photons that impinge upon it. The photon detection efficiency is defined as the probability of detecting a photon, depending on its wavelength. However, an increase in voltage when using SPADs can result in an elevated likelihood of registering false counts, primarily due to afterpulsing, i.e., unwanted secondary avalanches triggered following the detection of a primary avalanche, and noise, as higher voltage can lead to an increase in background noise.

3.1.5 Dark Count Rate

The dark count rate is the rate of signals where no light falls onto the detector. It represents the minimum counting rate of the detector[33][20]. The SPAD is in a metastable state until a photon strikes it. The dark count rate is caused by spontaneous avalanches in the metastable state spontaneous avalanches. By cooling the detector to a specific temperature, in this case about $-20\,^{\circ}\mathrm{C}$, one can regulate thermally generated dark counts. Every $8\,^{\circ}\mathrm{C}$ the detector is cooled, and the number of dark counts is reduced by a factor of 2. The dark count rate can also be reduced by minimizing the number of generation-recombination holes, the impurities of the material, and the defects of the crystal.

3.1.6 Afterpulsing

Time-correlated, spontaneously triggered avalanches are called afterpulses[33] [3]. During an avalanche, it is possible for charges to become trapped within the high electric field region. This occurs when an avalanche event takes place. These trapped charges have the potential to be released, leading to the initiation of another avalanche. These occurrences are referred to as afterpulses. There is an increase in the afterpulse rate when the delay in avalanche quenching prolongs. This is directly related to the excess bias voltage, where a high voltage amplifies the electric field within the detector. While the increased sensitivity resulting from excess bias voltage is advantageous for photon detection, it also elevates the probability of an afterpulse generation due to the extended active state within the detector.

3.2 SPAD Arrays

A SPAD array is an imaging technology that relies on a grid of pixels[15] [5]. Every individual pixel consists of a detector utilizing a single-photon avalanche diode, along with an analog pre-processing stage and digital electronics.

The main characteristics of an SPAD array are:

- Single-Photon Sensitivity: Each pixel of the array is highly sensitive and can detect individual photons, even in extremely low light conditions.
- High Resistance to Electronic Noise: The array can resist electronic noise interference, which ensures that the signals it detects remain reliable and accurate.
- High Frame Rate: The SPAD array can operate at a maximum frame rate of about 100,000 frames per second, with negligible dead times in between. However, the actual frame rate may vary depending on the specific design and intended application of the SPAD array. SPAD arrays can capture sequences of images rapidly, which is beneficial for real-time imaging.
- Efficient Photon Detection: The SPAD array can efficiently capture and register photons across various wavelengths within the visible spectrum. This makes it suitable for various imaging tasks, like fluorescence microscopy and spectroscopy.
- Reliable Performance in Varied Conditions: By sustaining a low dark count rate, which minimizes false detections, the SPAD array maintains accuracy even when subjected to room temperature conditions.
- Design Complexities: Every SPAD generates a digital pulse for every registered photon. This calls for intricate electronic circuitry at the individual pixel scale to effectively manage data handling, maintain temporal data within confined space, and maintain an acceptable fill factor.

3.3 Poisson Statistics of Photon Counting

The operation of a Geiger-mode avalanche photodiode involves two sequential unpredictable processes[4]. First, there's the production of initial electrons, which can occur in several ways, including:

- Absorption of laser photons.
- Absorption of background photons from natural light sources like sunlight.
- Internal thermal noise, which generates a dark current.

Following the generation of these initial electrons, the subsequent step encompasses the avalanche effect, triggered by one or possibly multiple initial electrons. This cascade results in the production of an unpredictable quantity of charge carriers.

The probability that m events occur during a time interval t_1 and t_2 is

$$P(m, t_1, t_2) = \frac{1}{m!} \left[M(t_1, t_2)\right]^m \exp(-M(t_1, t_2)) \tag{2}$$

where $M(t_1, t_2)$ indicates the probability of an event occurring between times t_1 and t_2

$$M(t_1, t_2) = \int_{t_1}^{t_2} r(t)\, dt \tag{3}$$

and $r(t)$ symbolizes the process's rate function. The event refers to the creation of a primary electron either by a dark current event in the SPAD, a stray light event or an intended laser pulse photon.
The probability that no primary electrons are created is

$$P_{noevent} = \exp((-M(t_1, t_2)) \tag{4}$$

The probability that one or more primary electrons are created is

$$P_{event} = 1 - \exp((-M(t_1, t_2)) \tag{5}$$

A Poisson process has two main properties: Firstly, the additivity property: When one adds together multiple independent random variables that follow Poisson distributions, the result is still a Poisson-distributed random variable. The average rate of this combined variable is the sum of the individual average rates. Secondly, the independence property: The occurrence of events within one specific time span remains completely unrelated to the events taking place in any other not overlapping time span.

3.4 Measuring the Quantum Efficiency of SPADs

Quantum efficiency describes how efficiently a photodetector can convert incoming photons of light into an electrical signal. It measures the device's ability to capture and utilize incoming photons.

In the paper titled 'A study to develop a robust method for measuring the detection efficiency of free-running InGaAs/InP single-photon detectors' [12], four institutes detail their experimental setups and findings for measuring the quantum efficiency of fiber-coupled indium gallium arsenide (InGaAs/InP) SPAD detectors. This paper is employed in this study because it presents various methodologies derived from their experiments for determining quantum efficiency. One of these methods is utilized in this thesis to experimentally ascertain the quantum efficiency in the laboratory setup. However, several adjustments are necessary to ensure compatibility with the experimental configuration in this study.

The measurement principle is based on the so-called substitution method. The approach involves a procedure in which the optical power, denoting the number of photons detected per second by the detector, is compared with the average optical power per laser pulse. The following equations are derived from the paper, and subsequent chapters will provide an explanation of each of its components while ensuring their compatibility with the laboratory setup.

$$\rho_{\text{click}} = f_{\text{laser}} \frac{q}{mq+1} \exp\left(-\rho_{\text{dark}} D\right) + \frac{\rho_{\text{dark}}}{1 + (q f_{\text{laser}} + f_{\text{laser}}) D} \tag{6}$$

$$q = 1 - \exp\left(-N_{\text{photon}} \eta_{QE}\right) \tag{7}$$

The Eq.6 and 7 incorporate various parameters. In this context, q represents the event rate ratio and will be derived in more detail later. The parameter f_{laser} is the repetition rate of a pulsed laser, ranging from 1 to 80 kHz. The parameter ρ_{click} indicates the rate of detected events on the detector. D represents the detector's dead time, which in the case of this study setup is 25 ns. The parameter ρ_{dark} is the counted dark count rate of the detector, which should range between 100 to 600 Hz, depending on the gain. The parameter m stands for the mode number, which in this study is $m = 0$, as it represents the fundamental mode. In the fundamental mode, the laser beam's intensity distribution in the beam's cross-section is the most symmetric. This means that the intensity of the beam is highest at the center and gradually decreases towards the edges. η_{QE} is the quantum efficiency for photon efficiency and is the parameter to be determined. Lastly, the parameter N_{photon} denotes the photon count of the Poissonian laser pulse on the SPAD. In the case of a 15 ns wide and intense Gaussian laser pulse, the detected spread of photons within the pulse duration can exceed 15 ns. The Gaussian time profile allows for a spread of photon arrivals within the pulse duration, giving the SPAD detector sufficient time to recover between detections. This phenomenon arises due to the time profile, which allows for a distribution of photon arrivals following a Gaussian curve. This means that photon arrivals are more likely to cluster around the pulse's peak intensity, causing a wider spread compared to a Poissonian laser pulse. In contrast, a Poissonian laser pulse exhibits a distinct behavior where photon arrivals follow a Poisson distribution, resulting in a more randomized pattern of photon arrivals within the pulse duration. Consequently, the spread of photon detections within a Poissonian pulse is typically more uniform and less clustered around the pulse peak.

Now looking at the two terms in Eq.6:

First Term:

$$\begin{aligned} \min : \rho_{\mathrm{dark}} D &= 100\,\mathrm{Hz} \times 25\,\mathrm{ns} = 2.5 \cdot 10^{-6} \\ \max : \rho_{\mathrm{dark}} D &= 600\,\mathrm{Hz} \times 25\,\mathrm{ns} = 1.5 \cdot 10^{-5} \end{aligned} \tag{8}$$

which leads to the first term being

$$\exp\left(\rho_{\mathrm{dark}} D\right) \approx 1. \tag{9}$$

Second Term:
There are two cases in the second term because q is unknown.
In case of a)

$$q f_{\mathrm{laser}} > \rho_{\mathrm{dark}} \Leftrightarrow q f_{\mathrm{laser}} D << 1 \tag{10}$$

because $f_{\mathrm{laser}} < 80\,\mathrm{kHz}$

$$80\,\mathrm{kHz} \times 25\,\mathrm{ns} = 0.002 \tag{11}$$

which leads to

$$\Rightarrow \rho_{click} = q f_{\mathrm{laser}} + \rho_{\mathrm{dark}} \tag{12}$$

In case b)

$$q f_{\mathrm{laser}} < \rho_{\mathrm{dark}} \tag{13}$$

which leads to the same result.

In the next step, Eq.12 is transformed and equated with Eq.7 and then q can be derived as

$$q = \frac{\rho_{\text{click}} - \rho_{\text{dark}}}{f_{\text{laser}}} = 1 - \exp\left(-N_{\text{photon}}\eta_{\text{QE}}\right) \tag{14}$$

The scaling of the uncertainty of the quantum efficiency η_{QE} vs. the uncertainty of the photon number N_{photon} is as follows:

$$\begin{aligned}
\eta_{\text{QE}} &= -\frac{\ln(1-q)}{N_{\text{photon}}} && (15)\\
\Rightarrow \frac{\partial \eta_{\text{QE}}}{\partial N_{\text{photon}}} &= \frac{\ln(1-q)}{N_{\text{photon}}^2} + \frac{1}{(1-q)\,N_{\text{ph}}}\frac{\partial q}{\partial N_{\text{photon}}} && (16)\\
&= \frac{\ln(1-q)}{N_{\text{photon}}^2} + \frac{\eta_{\text{QE}}\exp\left[-N_{\text{photon}}\eta_{\text{QE}}\right]}{(1-q)\,N_{\text{photon}}}\frac{\partial \eta_{\text{QE}}}{\partial N_{\text{photon}}} && (17)\\
&= \frac{\ln(1-q)}{N_{\text{photon}}^2} + \frac{\eta_{\text{QE}}}{N_{\text{photon}}}\frac{\partial \eta_{\text{QE}}}{\partial N_{\text{photon}}} && (18)\\
\Rightarrow \frac{\Delta \eta_{\text{QE}}}{\eta_{\text{QE}}} &= \frac{\Delta N_{\text{ph}}}{N_{\text{photon}}}\left[1 - \frac{\eta_{\text{QE}}}{N_{\text{photon}}}\right]^{-1} \approx \frac{\Delta N_{\text{photon}}}{N_{\text{photon}}} && (19)
\end{aligned}$$

This means that is not able to determine the quantum efficiency with higher precision than the precision to determine the photon number in the laser pulse.

4 Experimental Laboratory Setup

This chapter provides a detailed description of the experimental laboratory setup, including an explanation of its components. The primary objective was to employ a Single Photon Avalanche Detector to precisely locate and reliably detect laser pulses within specific range windows, utilizing the minimum number of photons possible, effectively shielding it from the background and stray light photons. In pursuit of this objective, extensive laboratory experiments were undertaken to examine the detector's behavior. A versatile configuration was employed, compromising a laser seed driver, PicoLAS BFS-VRM 03 HP, in tandem with an arbitrary pulse generator, PicoLAS PLCS-40, and a semiconductor laser diode. This arrangement facilitated the generation of laser pulses, exhibiting varied shapes, amplitudes, and duration, faithfully replication the conditions encountered in practical altimetry scenarios. A fiber equipped with electronic variable optical attenuators, bandpass filters, and other optical components delivered these laser pulses to a single photon counting detector, the Single Photon Detection Module with Adjustable Gain (SPDMA) from Thorlabs. To simulate representative optical noise, a light source was introduced through a Y-fiber.

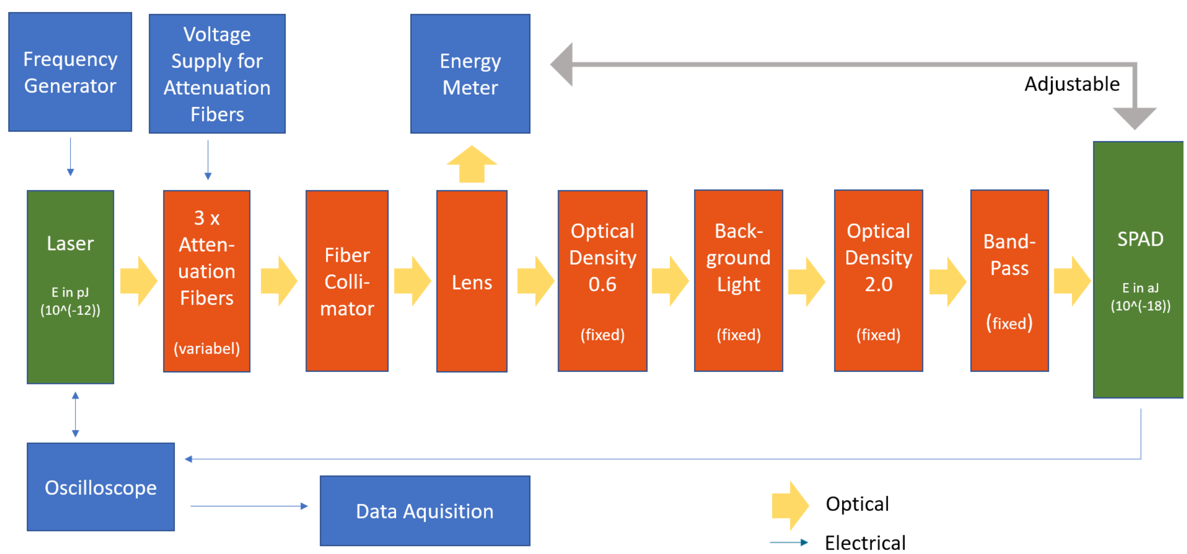

Abbildung 15: **Schematic structure of the experimental laboratory setup.** The Laser and SPAD are in green, the laboratory equipment for optical measurement is in blue and the optical setup to minimize the number of photons per laser pulse is in orange. The yellow arrows represent optical light and the blue arrows represent electrical connections.

Fig.15 illustrates the schematic structure of the experimental laboratory setup, and Fig.16 displays an actual image of the experimental laboratory setup employed in this study. The starting point of the setup is represented by the laser, which is connected to a laser pulse generator and an oscilloscope. The laser pulse generator is responsible for controlling the pulse repetition frequency of the laser, while the oscilloscope captures the digital signals from the devices being measured, including the set voltages of the attenuators, the voltages of the laser pulses, and the voltages of the detector, using one or more input channels The oscilloscope software processes the signal data and displays the resulting waveform on the screen, allowing for easy visualization and analysis. A precise optical arrangement is implemented to guide the laser pulse to minimize the photon count per pulse. Initially, the setup incorporates three attenuators, each controlled by a voltage supply. Each voltage setting corresponds to a specific level of laser beam attenuation, reducing the number of photons. Following the attenuators are a collimator and a lens, along with two optical densities and a bandpass filter. The collimator and lens are used to focus the laser pulse. At the same time, the density filters reduce the intensity of the pulse, and the bandpass filter enables the detection of a specific wavelength. Ultimately, the detector is positioned after the filter. The setup is designed to accommodate both the detector and an energy meter on a single plate, allowing them to be interchanged by adjusting the plate's position based on specific requirements. The energy meter measures the laser beam energy later, both with and without optical components.

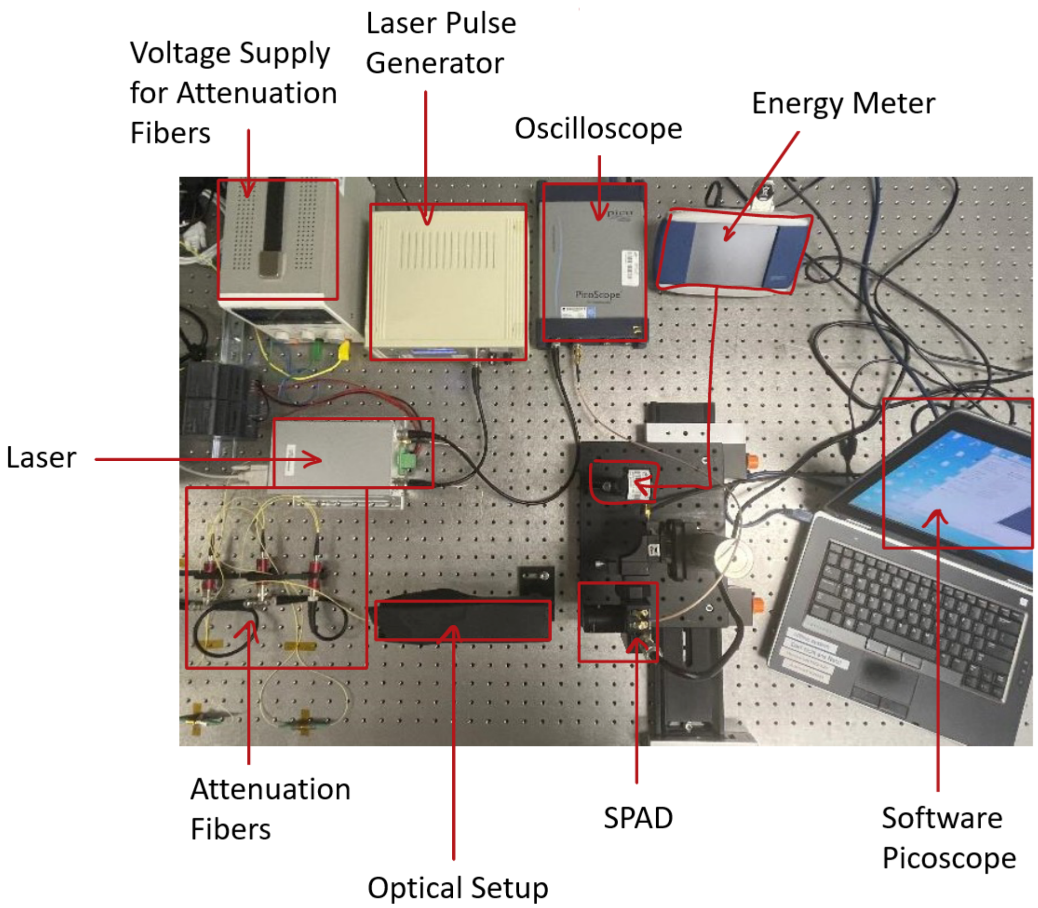

Abbildung 16: **Picture of the official experimental setup in the laboratory.** Same as in Fig.15 but as an actual photograph of the laboratory setup.

4.1 Laser Diode

A 1064 nm single-mode 14-pin butterfly module laser diode is used in the experimental setup[27][17]. This particular laser diode is housed within a butterfly-shaped package containing 14 pins, as shown in Fig.17. The butterfly package serves a dual purpose by providing essential mechanical support and efficient thermal management for the laser diode. This means that the butterfly package helps dissipate the heat generated by the laser diode, preventing it from overheating and ensuring stable performance. These 14 pins establish electrical connections to the laser diode and monitor its performance.

The laser diode possesses a short rise time of 1 ns and operates at a wavelength of 1064 nm. The term single mode signifies that the laser emits radiation in a single spatial mode, specifically the fundamental mode, effectively disregarding the influence of higher-order modes. This characteristic results in the generation of a focused beam with minimal divergence.

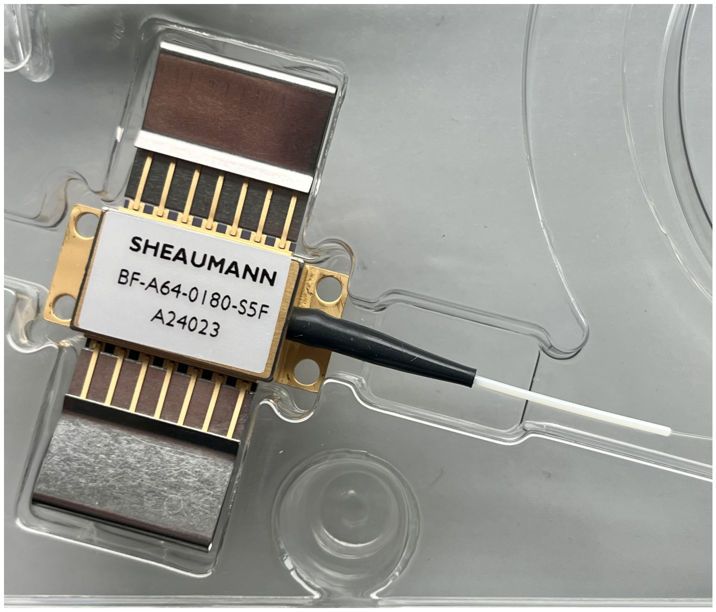

Abbildung 17: **The 1064 nm single-mode 14-pin butterfly module laser diode used in the experimental setup from sheaumann**

Furthermore, the operation and modulation of this laser diode are managed by two essential components: the BFS-VRM 03 HP power supply unit provided by PicoLAS and the PLCS-40 Pulse Generator, also from PicoLAS. The BFS-VRM 03 HP Seed Driver allows precise control over laser pulse duration, from picoseconds to continuous wave mode. It is designed for Seed Diodes in solid-state and fiber lasers, offering analog modulation and ultra-short picosecond pump pulses with a minimum pulse duration of 1 ns. The PicoLAS PLCS-40 is an advanced pulse generator with 32 programmable waveform shapes, spanning pulse duration from 5 to 320 ns. It is an ideal companion for the laser diode driver used in this study and is suitable for seed laser diodes, material processing, and distance measurement applications.

4.2 Thorlabs SPDMA

The Single Photon Detection Module with adjustable gain (SPDMA) is used for the experimental setup[33]. The detector used in the laboratory setup is shown in Fig.18 and 19, once without in Fig.18 and once within Fig.19 the added optical elements in front of the detector. The SPDMA is a specific type of Single Photon Detector (SPD), which can be used for wavelengths between 350 nm and 1100 nm, so it can detect wavelengths up to the near-infrared. Fig.20 illustrates the efficiency of the detector. On the y-axis, the probability detection efficiency is expressed in percentage, while the corresponding wavelength is plotted on the x-axis. The red curve represents the detector's efficiency at maximum gain, whereas the blue curve represents minimum gain. At a wavelength of 600, nm and maximum gain, the SPDMA from Thorlabs achieves its highest photon detection efficiency, approximately 50% higher than when operating at minimum gain. The detector consists of a silicon avalanche diode and is constantly cooled to a temperature of $-20\,^{\circ}\mathrm{C}$ by an integrated Thermo Electric Cooler. The SPDMA is designed with a feature that allows users to control its gain settings. This adjustability leads to the choice between optimizing photon detection efficiency for enhanced sensitivity to low-intensity signals or reducing the probability of dark counts, which are signals recorded without actual photon detections. By adjusting the gain, one can achieve either a heightened sensitivity to weak light signals or a minimized likelihood of registering dark counts. Detected photons are transformed into a TTL pulse within the detector, which are binary and have only two states: high, which corresponds to about 5 V and low, which corresponds to about 0 V. The SPDMA has an active area with a diameter of $500, \mu$m, and an integrated connection, which allows for direct observation of the module's signal on an oscilloscope.

Abbildung 18: **Picture of the SPDMA from Thorlabs used in the laboratory setup.** Without the optical components in front of the detector.

Abbildung 19: **Picture of the SPDMA from Thorlabs used in the laboratory setup.** With the optical components: the 2.0 and 0.6 optical densities and the bandpass in front of the detector.

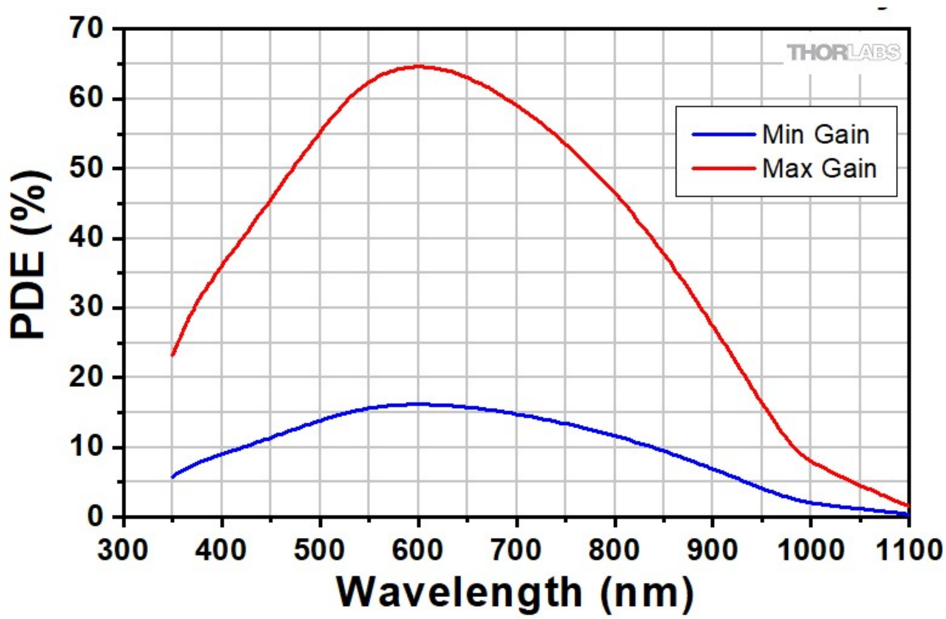

Abbildung 20: **The photon detection efficiency of the SPDMA from Thorlabs.** The y-axis represents the photon detection efficiency, and the x-axis represents the wavelength. The blue curve displays the detection efficiency of the detector at minimum gain, while the red curve displays it at maximum gain. The highest detection efficiency is achieved at a wavelength of 600 nm and maximum gain setting.

4.3 Attenuation Fibers

Attenuation fibers are used in the experimental setup to reduce the intensity of the light signal transmitted through the fiber[31]. The fiber-coupled Electronic Variable Optical Attenuators (VOAs) (Fig.24) allow for precise control of signal strength in single-mode fibers, and they increase the reliability and the reproducibility in the experimental setup.

Operation principle of the attenuation fibers: The attenuators utilize specialized mirrors strategically tilted at precise angles in the fiber. When an incoming light signal passes through the fiber, these mirrors reflect a portion of the signal. The title angle of the mirrors determines the proportion of the reflected light that is guided out of the fiber. This parameter, the tilt angle, is controlled by applying voltage to the attenuator. Fundamentally, by varying the voltage applied to the attenuator, the angles of the mirrors are adjusted accordingly. As a result, the amount of signal diverted out of the fiber can be finely tuned, allowing for precise control over signal strength. This level of control is invaluable in optimizing optical systems, as it enables the tailoring of signal strength to meet specific requirements, minimizes unwanted signal noise, and ultimately enhances the overall reliability and performance of optical systems.

Fig.24 illustrates the V1000 attenuating fiber used in this study. The device is equipped with a single-mode optical fiber designed for use within the specified operating wavelength range. Optical transmission is controlled by applying driving voltages ranging from 0 to 5 V, reducing optical output as the voltage increases. One end features components (in red) responsible for light attenuation and includes a BNC connector that connects to the voltage generator. At the other end are two yellow fibers, one for receiving the laser light and the other for coupling it into another fiber attenuator or the optical setup.

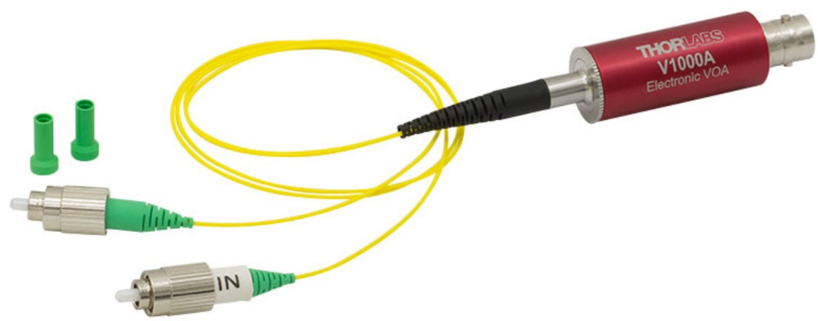

Abbildung 21: **Attenuation Fiber V1000A from Thorlabs.** The yellow cables contain the components for light attenuation, achieved by tilting a mirror within the fiber. The red electronic box at the end of the fiber is responsible for controlling the attenuation process, including the adjustment of the mirror's tilt angle to achieve the desired attenuation level[31].

4.4 Optical Setup

The optical setup plays an essential role in the experimental configuration, as it is integral to the objective of further reducing the number of photons per laser beam. This optical setup consists of a 1064 nm fiber collimator, a lens, two optical density filters, and a bandpass filter. Together, these components are strategically employed to control the photon count within the laser beam precisely.

4.4.1 Fiber Collimator

A 1064 nm fiber collimator, like the F810 Series fiber collimation Package used in the laboratory setup from Thorlabs, is designed to efficiently couple a laser beam propagating from the end of an optical fiber into the surrounding environment[30]. This is demonstrated in Fig.22 and 23, where the coupled fiber (in green) to the collimator can be observed in the laboratory setup. The collimators are pre-aligned to ensure the laser beam is effectively collimated when it exits the fiber. The F810 Serie Fiber Collimation Packages are designed to work within a range of wavelengths from 405 nm to 2 μm. However, they are optimized for their best performance at the specified wavelength -

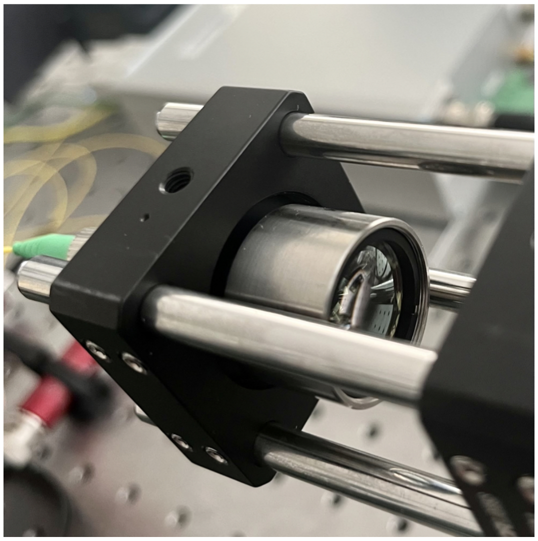

Abbildung 22: **The 1064 nm fiber collimator in the laboratory setup.** The fiber is in yellow and couples (in green) into the collimator in the black frame for mounting.

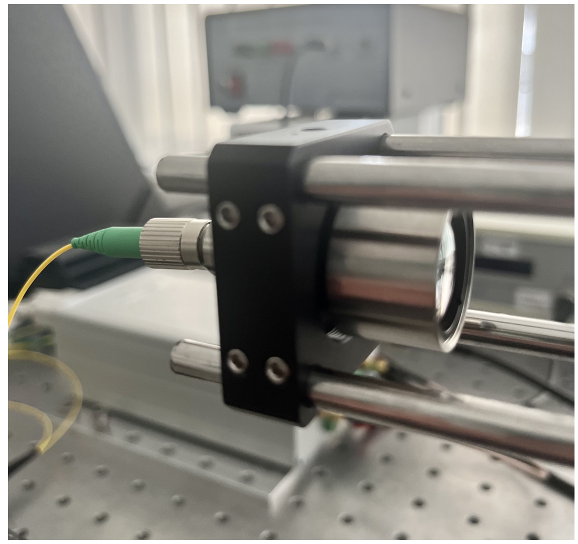

Abbildung 23: **The 1064 nm fiber collimator in the laboratory setup.** The fiber is in yellow and couples (in green) into the collimator in the black frame for mounting..

in this case, 1064 nm. These collimators utilize a multi-element lens design to achieve diffraction-limited performance. This means they produce a laser beam with minimal divergence, producing a well-collimated and precise output.

4.4.2 Lens

In the optical setup, a transparent material is used for the lens, shaped to focus incoming light[7]. Lenses operate by bending or refracting light as it traverses through the material, altering the direction of light rays and guiding them to converge, ultimately focusing on the SPAD detector. The lens's specific design and characteristics are carefully tailored to manipulate the incoming wavefront, ensuring alignment with its intended role within the optical system.

Thorlabs N-BK7 [34] lenses are expertly engineered to minimize spherical aberration while maintaining spherical surfaces for lens formation. They deliver exceptional performance, particularly in the collimation and focusing of light beams. The lens in the laboratory setup has a focal length of 100 mm, complementing its design parameters which include a convex/convex lens shape and an N-BK7 material, which is a type of optical glass, suitability for high-power applications, and the ability to achieve diffraction-limited performance even at small input diameters[**?**]

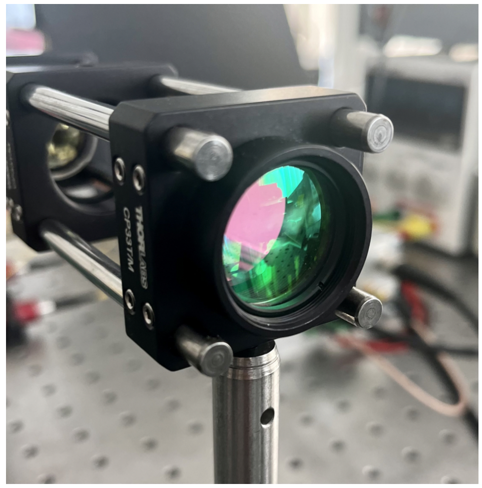

Abbildung 24: **The lens used in the optical setup in the laboratory.** A lens is a transparent material that focuses incoming light and is held in a black frame for mounting.

4.4.3 Optical Densities

Optical density (OD) is defined as the logarithm to the base 10 of the attenuation factor by which the optical filter attenuates the laser power[24]. For example, an OD of 3 leads to a reduction of the laser light of 1000 times. Optical densities are needed to decrease the number of photons detected by the SPAD.

4.4.4 Bandpass

A bandpass is a filter that only allows a specific range of wavelengths to pass through while attenuating wavelengths outside that range[32]. A bandpass is characterized by its center wavelength, the wavelength at which the filter has the maximum transmission, and its bandwidth, which is the range of wavelengths the filter allows to pass through with minimal attenuation. In the laboratory setup, the used bandpass filter has a bandwidth of 3 nm and a center wavelength of 1064 nm with a diameter of 25 mm. The transmission and optical density plots of the bandpass FLH1064-3 from Thorlabs are shown in Fig.25. Fig.(a) shows the transmission on the y-axis and the wavelength on the x-axis. One can observe that only the wavelength 1064 nm with a bandwidth of 3 nm is transmitted, while all other wavelengths are filtered out. One can see the optical density on the y-axis of Fig.(b), while the x-axis displays the wavelength. This type of plot called an OD plot, shows how much light is absorbed in different wavelengths and how well the filter blocks light outside the transmission band. The absorption is highest except at the wavelength of 1064 nm.

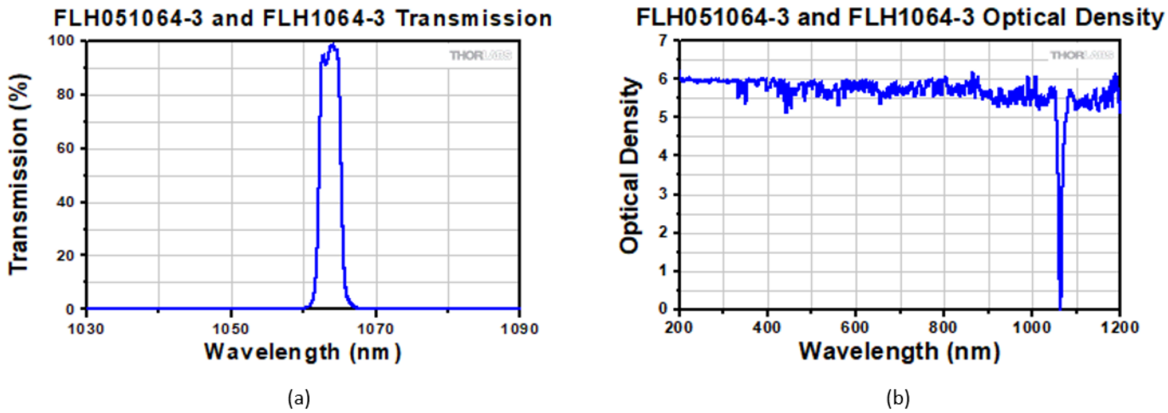

Abbildung 25: **The transmission and optical density plot of the 1064 nm bandpass filter.** (a) shows the transmission plot and (b) the optical density plot of the bandpass used in the experimental setup. The OD plot represents the absorption characteristics of the filter, whereas a transmission plot illustrates how effectively the filter allows light to pass at different wavelengths[32].

4.5 Data Acquisition with Picoscope

The software application PicoScope 6, developed by Pico Technology, is used in the laboratory. PicoScope 6 is a powerful tool to control and utilize PicoScope devices effectively. It can undertake diverse tasks encompassing signal acquisition, analysis, and visualization.

After launching the PicoScope software on the computer and connecting it to the PicoScope device via USB, the input channels for data acquisition need to be chosen. In the laboratory, these channels were linked to measuring voltage, laser activity, and the SPAD responses. The PicoScope is an oscilloscope that captures electrical signals when a trigger is activated. This trigger can be initiated by a start button, at a specific time interval, or in response to a laser pulse. The real-time data is then saved in a text file for further analysis.

To analyze the data, a specialized program was developed in Python. The PicoScope now has the measurement data stored in a text file. This file contains three sets of information: the time stamp, the laser voltage, and the detector voltage. One can configure how frequently and for how long these measurements are taken. However, the PicoScope has a specific storage capacity that cannot be exceeded. Because of this limitation, measurements can be repeated multiple times instead of running them continuously. A time interval of 0.8, ns was selected for data acquisition, implying that data points were captured at intervals of 0.8, ns. For example, if the measurement duration was extended to $1\,\mu$s, then $\frac{1\,\mu\text{s}}{0.8\,\text{ns}} = 1250$ timestamps were conducted in this measurement.

The developed program was integrated into an existing program in Python, used for the operational ground support equipment data of GALA. This pre-existing program organizes the data of the PicScope into new folders so one can work with it effectively. The newly developed program for this work is designed to analyze and evaluate the SPAD data, establishing a temporal context, and proceeds through a series of steps:

1. The program examines the values in the lists of laser and detector data in the text files.

2. If a pre-set threshold is exceeded in the values, the program records the corresponding time values. The program looks for transitions in the values. In the case of the laser, a transition indicates the laser pulse is emitted, and in the case of the detector, it signifies a detection event.

3. The program now focuses solely on the detector data. It refines the data further and generates a plot with all individual measurements on the x-axis and time on the y-axis. This means one can now see the timing relationships of all detections across the measurements.

4. Different time intervals can now be configured for analysis. This helps in examining how quickly events are detected one after another, allowing to distinguish signal photons from laser afterpulses, background photons, or dark counts.

5 Measurements and Results

5.1 Determination of the Dark Count Rate

The initial measurement aimed to determine the dark event rate of the utilized detector within the experimental setup, specifically, the rate at which events occur without exposing the detector to light. On average, dark events were expected to occur at regular intervals, and this time interval can be determined using the Poisson equation 21. The Poisson method is a statistical approach used to calculate the probability of discrete events occurring within a constant average interval. The probability P of k events occurring in a time interval t as a function λ is given by

$$P(k,\lambda) = \frac{\lambda^k}{k!} e^{-\lambda} \tag{20}$$

$$= \frac{1}{k!} \left(\frac{t}{t_{\text{mean}}} \right)^k \exp\left(-\frac{t}{t_{\text{mean}}} \right) \tag{21}$$

where the parameter λ describes a relative number of events for an observation. The required factor in the formula is denoted as t_{mean}, which represents the average time interval of a dark event.

According to the SPAD datasheet [17], the dark event rate has been determined to typically be of the order of 300 Hz, which means $t_{\text{mean}} = 3,\bar{3}\,\text{ms}$. Measurements were conducted for various time durations to ascertain this average time between dark events.

In Fig.26 and Fig.27, a series of measurements were carried out throughout $t = 10\,\text{ms}$ and $t = 100\,\text{ms}$, set on the PicoScope. On the x-axis is the total number of detected events in the time interval. On the y-axis is the probability of expecting this number of events. A total of 2,000 measurements were conducted to gather the necessary data. Fig.26 and Fig.27 show the distribution of events detected during these measured time intervals, with the red bars representing the frequency of occurrences, i.e., it was observed that the most frequent number of events were 7 detections, detected within a 10 ms interval. By fitting the Poisson formula to the results, it became possible to determine the number of dark events.

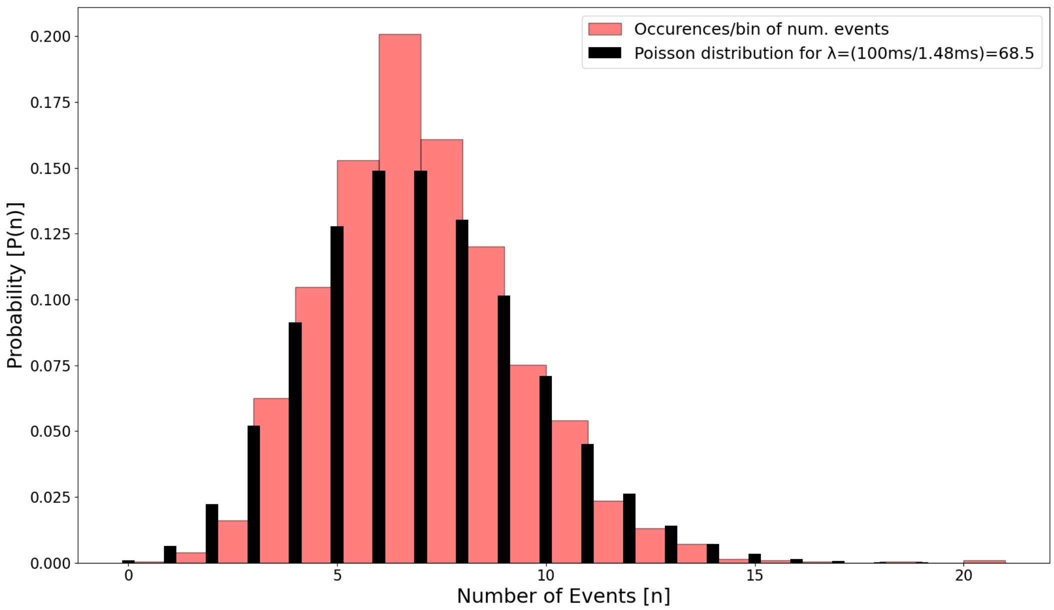

Abbildung 26: **Dark Count Rate Measurement 2000 times for t=10 ms.** On the y-axis is the probability for expecting a specific number of events in the time interval of 10 ms, and on the x-axis is the specific number of detected events. In yellow are the occurrences per bin of the number of detected events in the measurement, and in black is the Poisson distribution fitted to the data.

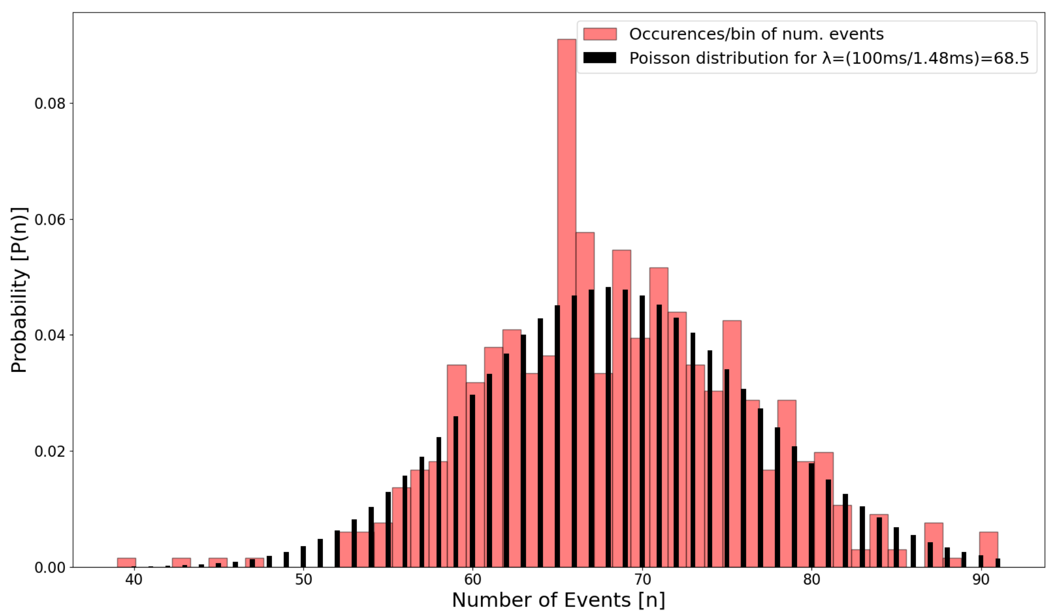

Abbildung 27: **Dark Count Rate Measurement for t=100 ms.** Same as in Fig.25, but for 100 ms.

To determine the parameter t_{mean}, the Poisson distribution was employed for a fitting procedure, as represented by the black bars in the plot. By rearranging the equation

$$\lambda = \frac{t}{t_{\text{mean}}} \tag{22}$$

the desired value of t_{mean} was derived, with the understanding that t remains constant.

In the plot representing a time interval of $t = 100, \text{ms}$, a calculated value of $t_{\text{mean}} = 1.48\,\text{ms}$ is evident, indicating that dark events occur every 1.48 ms. However, the value decreases when analyzing smaller time intervals. For instance, in the plot representing a time interval of $t = 10\,\text{ms}$, t_{mean} reduces to 1.43 ms. This reduction in t_{mean} at smaller time intervals can be attributed to the statistical nature of the data, where the limited number of observed events in shorter intervals introduces more significant variability and uncertainty into the calculations and in shorter time intervals, typically only the pulses that are closer together are counted. The measurements were conducted only at maximum gain, as the rate of dark counts was already higher, according to the data sheet than at minimum gain.

5.2 Determination of the Detected Photon Number and Quantum Efficiency as a Function of Detector Gain

In the characterization of the detector, the subsequent step involved two tasks: First, quantifying the number of photons incident on the laser per pulse N_{photon} within the laboratory setup, and second, determining the quantum efficiency η_{QE} of the detector. The quantum efficiency values were examined to the gain parameter, which affects the detector's sensitivity.

The experiment measured the number of events and detected signals on the SPAD while varying the voltage passing through the attenuators. As the voltage was increased, fewer photons were observed to pass through the system. Each voltage value corresponds to a transmission that is given in the data sheet.

In this chapter, one will frequently encounter the terms photons,signal photons,events,änd ëvent rate ratio."While these terms share a similar foundation, they have different meanings. The term photonsrelates to the quantity of photons emitted by the laser per pulse. SSignal photons"denotes explicitly the number of photons sent by the laser pulse when considering the laser's quantum efficiency later on. Ëventsrepresent the count of detected occurrences at the detector. And Ëvent rate ratiorefers to the relationship between emitted laser pulses and detected events."

5.2.1 Measuring the Laser Pulse Energy

Before starting the measurement, the laser pulse energy was precisely measured using an energy meter, while maintaining a fixed voltage setting on the attenuator and without employing optical densities or a bandpass filter. This measurement served as a reference value for the energy at that specific voltage, essential for subsequent calculations.

The reference values obtained from this measurement are represented in the equation

$$\frac{E_{\text{known}}}{\tau_{\text{known}}} = \frac{E_{\text{puls}}}{\tau_{\text{total}}} \tag{23}$$

where τ_{known} represents the set transmission of the three attenuators, at which the energy E_{known} of the laser pulse is measured with the energy meter. The parameter τ_{total} pertains to the transmission values of all optical components placed before the SPAD, including the three attenuators, denoted as τ_{U}, where each τ_{U} represents the same value applied to all three attenuators τ_{U_1}, τ_{U_2}, and τ_{U_3}. Additionally the transmission of the bandpass τ_{BP}, which will also be measured, and the transmissions of the optical densities $\tau_{\text{OD}_{2.0}}$and $\tau_{\text{OD}_{0.6}}$. The factor τ_{total} allows for the measurement of the corresponding energy of the laser pulse, E_{pulse} when the pulse is attenuated with all components.

$$\Leftrightarrow E_{\text{pulse}} = \frac{E_{\text{known}}}{\tau_{\text{known}}}\tau_{\text{total}} \tag{24}$$

$$\Leftrightarrow E_{\text{pulse}} = \frac{E_{\text{known}}}{\tau_{\text{known}}}\tau_{\text{U}_1}\tau_{\text{U}_2}\tau_{\text{U}_3}\tau_{\text{BP}}\tau_{\text{OD}_{2.0}}\tau_{\text{OD}_{0.6}} \tag{25}$$

$$\Leftrightarrow E_{\text{pulse}} = \frac{E_{\text{known}}}{\tau_{\text{known}}}\tau_{\text{U}}\tau_{\text{BP}}\tau_{\text{OD}_{2.0}}\tau_{\text{OD}_{0.6}} \tag{26}$$

To determine the number of photons per laser pulse, the energy of the pulse should be divided by the energy of a photon at the wavelength of 1064 nm. The energy of a photon can be determined using the equation

$$E_{\text{photon}} = h\nu = h\frac{c}{\lambda} = 1.9 \cdot 10^{-19}\text{J} \tag{27}$$

where $h = 6.63 \cdot 10^{-34}$Js is the Planck constant and λ is the wavelength. This leads to the final equation for the photon number per pulse

$$N_{\text{photon}} = \frac{E_{\text{pulse}}}{E_{\text{photon}}} \tag{28}$$

The values of the laser pulse energy were measured at the voltage $U_{\text{known}} = (2.9 \pm 0.001)\text{V}$, corresponding to a transmission of $\tau_{\text{known}} = 0.1595 \pm 0.0005$ and the corresponding measured energy is $E_{\text{known}} = (0.1 \pm 0.004)\text{pJ}$.

The subsequent step involved measuring the transmissions of the optical densities and the bandpass. This was done by directly comparing the energies both with and without optical densities and filters. The result was a transmission of $\tau_{OD_{2.0}} = 0.031 \pm 0.04$, τ at the optical density of 2.0, a transmission of $\tau_{OD_{0.6}} = 0.29 \pm 0.04$ at the optical density of 0.6 and a transmission of $\tau_{BP} = 0.913 \pm 0.04$ for the 1064 nm bandpass filter.

5.2.2 Calculation of the Uncertainty of the Energy

The uncertainty in energy E_{pulse} Eq.26 and thus the uncertainty in the number of photons per laser pulse N_{photon} Eq.28 are determined through the propagation of uncertainty method. The variables E_{known}, TR_{BP}, $TR_{\text{OD}_{2.0}}$ and $TR_{\text{OD}_{0.6}}$ all share the same relative uncertainty, which is the uncertainty of the energy meter (4%)

$$\Delta E_{\text{known}} = 0.04 \times 0.1 \cdot 10^{-12}\text{J} = 4 \cdot 10^{-15}\text{J} \tag{29}$$

$$\Delta TR_{\text{BP}} = 0.04 \times 0.913 = 0.03652 \tag{30}$$

$$\Delta TR_{\text{OD}_{2.0}} = 0.04 \times 0.031 = 0.00124 \tag{31}$$

$$\Delta TR_{\text{OD}_{0.6}} = 0.04 \times 0.29 = 0.0116 \tag{32}$$

except for the uncertainty of τ_U, since it is a function of the voltage U and needs to be individually calculated.

The datasheet of the attenuators provided a corresponding transmission value for each voltage. From this data, a graph could be generated by plotting the voltages and the corresponding transmissions that were relevant to the task, which is illustrated in Fig.28. The curve was then fitted with a 6th-degree polynomial function, which is displayed in the top right corner.

To calculate the uncertainties of the attenuators, one needs to compute the derivative of the function and then evaluate the following formula

$$\Delta\tau_{\mathrm{U}} = \frac{\partial\tau(U)}{\partial U}\bigg|\Delta U \tag{33}$$

where ΔU represents the known uncertainty of 0.001 V from the voltage measurement device.

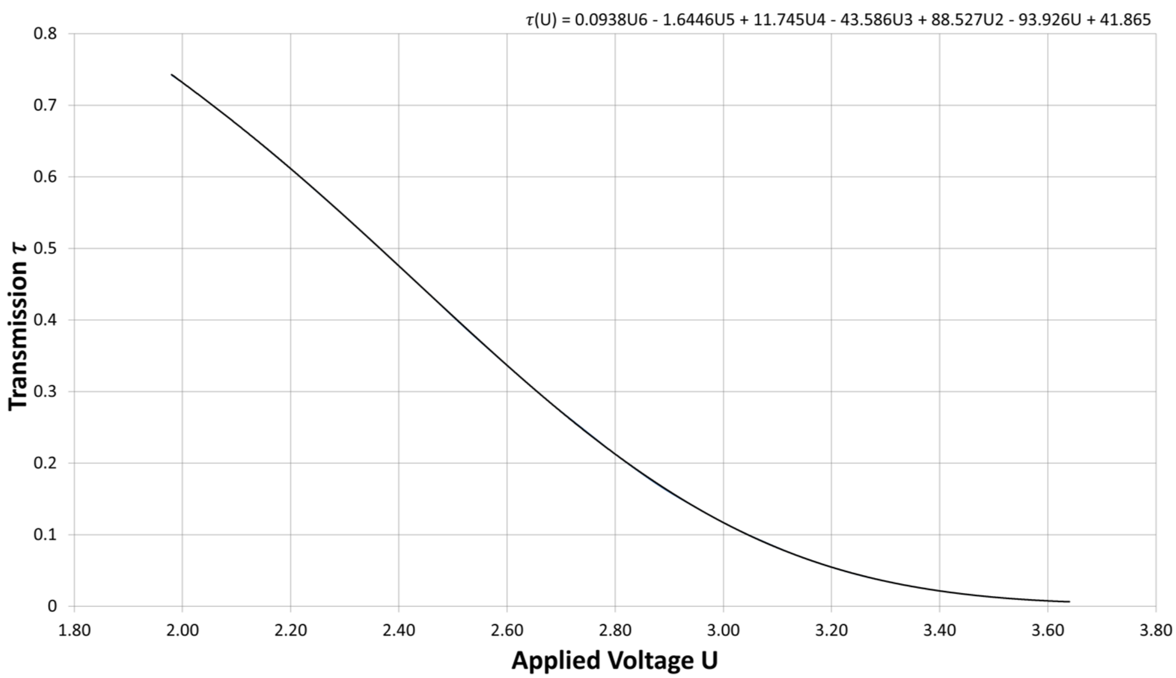

Abbildung 28: **The voltage against the corresponding transmissions.** On the x-axis is the applied voltage of the attenuators and on the y-axis are the transmission values. A curve was fitted to the values and the function $\tau(U)$ is displayed in the right corner.

The following equation is the propagation of uncertainty for the value E_{pulse} as a function of U

$$\Delta E_{\mathrm{Pulse}}(U) = \sqrt{\left(\frac{\partial E_{\mathrm{Pulse}}}{\partial E_{\mathrm{known}}}\Delta E_{\mathrm{known}}\right)^2 + \left(\frac{\partial E_{\mathrm{Pulse}}}{\partial \tau_{known}}\Delta\tau_{\mathrm{known}}\right)^2 + 3\left(\frac{\partial E_{\mathrm{Pulse}}}{\partial \tau_{\mathrm{U}}}\Delta\tau_{\mathrm{U}}\right)^2} \tag{34}$$

$$\overline{+\left(\frac{\partial E_{\mathrm{Pulse}}}{\partial \tau_{\mathrm{BP}}}\Delta\tau_{\mathrm{BP}}\right)^2 + \left(\frac{\partial E_{\mathrm{Pulse}}}{\partial \tau_{\mathrm{OD}_{2.0}}}\Delta\tau_{\mathrm{OD}_{2.0}}\right)^2 + \left(\frac{\partial E_{\mathrm{Pulse}}}{\partial \tau_{OD_{0.6}}}\Delta\tau_{OD_{0.6}}\right)^2} \tag{35}$$

With the uncertainty in energy, it was also possible to calculate the uncertainty in the number of photons

$$\Delta N_{\text{photon}} = \frac{\Delta E_{\text{known}}}{\Delta E_{\text{photon}}} \tag{36}$$

The uncertainty calculation was thereby concluded for the number of photons per pulse.

5.2.3 Illustrating the Relationship Between the Event Rate Ratio and the Number of Detected Events

The primary objective is to illustrate the relationship between the parameter q representing the event rate ratio, and the number of photons detected by the detector. A plot will be created to visualize this relationship in the next step. The measuring process began at a voltage of $(3.5 \pm 0.001)V$ corresponding to a transmission of 0.01252 ± 0.0001. The detector was fed with a laser pulse 100,000 times and the number of events on the detector per measurement was recorded. The voltage U of the attenuators in the experimental setup was then gradually reduced in small steps, which means that the transmission was increased, and the procedure repeated until reaching a voltage of $(2.7 \pm 0.001)V$ corresponding to a transmission of 0.2724 ± 0.0006. The measurements were conducted twice, once at maximum gain and once at minimum gain.

After completing the measurements, the dataset now contains information on the number of detected events at the SPAD for various transmission values in the laboratory setup, which are shown in table 1. The table shows the voltage values of the attenuators, the corresponding transmissions and the number of detected events at maximum and minimum gain. The measurements were conducted with both the maximum and minimum gain settings of the detector. The observations show that the number of events per measurement increases with higher transmission values. Additionally, a substantial increase in the number of detected events on the SPAD is observed when operating at the maximum gain setting.

U [V]	τ	**Events @ min gain**	**Events @ max gain**
3.551	0.00976	84	431
3.501	0.01252	149	751
3.451	0.01636	307	1537
3.401	0.02152	654	3063
3.351	0.02793	1140	6457
3.29	0.03499	2411	11324
3.251	0.0435	4573	19851
3.201	0.05434	8054	33911
3.151	0.06683	15280	53890
3.1	0.08224	24998	73951
3.05	0.09879	39350	91108
3.001	0.1168	57681	98836
2.95	0.1375	80677	99981
2.9	0.15954	91559	100171
2.85	0.18461	98343	-
2.801	0.21224	99862	-
2.751	0.24194	99980	-
2.7	0.2724	99985	101219

Tabelle 1: **Set transmission τ and detected events at minimum and maximum gain.** The table displays the voltage values of the attenuators alongside their corresponding transmissions and the number of detected events at maximum and minimum gain.

5.2.4 Calculating the Number of Photons per Laser Pulse

Now the calculation of the energy of the laser pulses is required to accurately determine the number of photons per pulse. This information is vital for understanding the setup's performance and its ability to detect and quantify photons effectively. This computation will be performed using Eq.23. Table 2 presents the results of the calculations, illustrating the relationship between the number of photons per pulse, the energy of the laser pulse, and the transmission and voltage of the attenuators for every transmission value.

U [V]	τ	$\Delta\tau$	E_{pulse} [J]	ΔE_{pulse} [J]	N	ΔN
3.551	0.00976	0.00011	$1.91 \cdot 10^{-19}$	$3.95 \cdot 10^{-22}$	1	0.002
3.501	0.01252	0.00013	$4.03 \cdot 10^{-19}$	$8.27 \cdot 10^{-22}$	2	0.004
3.451	0.01636	0.00014	$8.99 \cdot 10^{-19}$	$1.83 \cdot 10^{-21}$	5	0.01
3.401	0.02152	0.00016	$2.05 \cdot 10^{-18}$	$4.16 \cdot 10^{-21}$	11	0.022
3.351	0.02793	0.00018	$4.47 \cdot 10^{-18}$	$9.07 \cdot 10^{-21}$	24	0.048
3.29	0.03499	0.00022	$8.79 \cdot 10^{-18}$	$1.78 \cdot 10^{-20}$	46	0.094
3.251	0.0435	0.00024	$1.69 \cdot 10^{-17}$	$3.41 \cdot 10^{-20}$	89	0.18
3.201	0.05434	0.00027	$3.29 \cdot 10^{-17}$	$6.65 \cdot 10^{-20}$	173	0.35
3.151	0.06683	0.00031	$6.12 \cdot 10^{-17}$	$1.24 \cdot 10^{-19}$	322	0.65
3.1	0.08224	0.00035	$1.14 \cdot 10^{-16}$	$2.30 \cdot 10^{-19}$	601	1.211
3.05	0.09879	0.00039	$1.98 \cdot 10^{-16}$	$3.99 \cdot 10^{-19}$	1041	2.098
3.001	0.1168	0.00043	$3.27 \cdot 10^{-16}$	$6.58 \cdot 10^{-19}$	1721	3.465
2.95	0.1375	0.00047	$5.33 \cdot 10^{-16}$	$1.07 \cdot 10^{-18}$	2808	5.651
2.9	0.15954	0.00051	$8.33 \cdot 10^{-16}$	$1.68 \cdot 10^{-18}$	4386	8.824
2.85	0.18461	0.00055	$1.29 \cdot 10^{-15}$	$2.60 \cdot 10^{-18}$	6795	13.668
2.801	0.21224	0.00058	$1.96 \cdot 10^{-15}$	$3.94 \cdot 10^{-18}$	10325	20.763
2.751	0.24194	0.00062	$2.91 \cdot 10^{-15}$	$5.84 \cdot 10^{-18}$	15295	30.749
2.7	0.2724	0.00065	$4.15 \cdot 10^{-15}$	$8.34 \cdot 10^{-18}$	21829	43.877

Tabelle 2: **Set transmission τ and resulting energy E_{pulse} and photon number N.** The table represents the number of photons per laser pulse at the respective transmissions. These values are unaffected by the detector's gain. The uncertainty in voltage is consistently 0.001 V.

On the basis of the above measurements, the energies and the associated number of photons per laser pulse were calculated. This is no longer dependent on the detector and therefore independent of the gain. The results are summarized in Fig.29, where the x-axis represents the transmission value of the attenuator and the y-axis the photon count per laser pulse. The scatter points on the graph correspond to the calculated data points and the plotted curve represents a fitted function that captures the relationship between the transmission values and the number of photons per laser pulse. Notably, the form of the fitted function indicates a cubic relationship, reflecting a third-degree polynomial connection. It is evident that the smaller the transmission, the lower the number of photons per pulse. As expected, the number of photons per laser pulse increases with the degree of transmission.

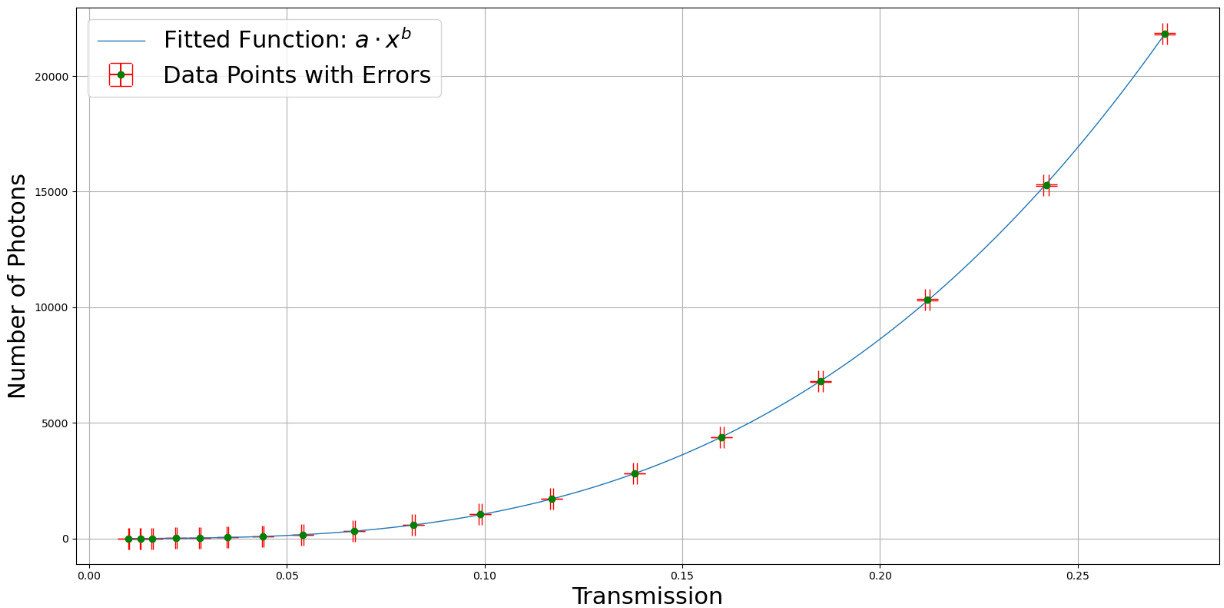

Abbildung 29: Visual relationship between the transmission of the attenuator and the number of photons per pulse

5.2.5 Calculating the Event Rate Ratio

The next step is the calculation of the event rate ratio, denoted as q. This ratio is determined by dividing the number of detected events by the total number of laser pulses directed at the detector during the measurement, represented by $N_{laser} = 100,000$.

$$q = \frac{\text{Events}}{N_{\text{Laser}}} \tag{37}$$

One can rely on statistical principles to evaluate the uncertainty associated with this event rate ratio. Since the number of detected events follows a Poisson distribution due to the random nature of the events, it is reasonable to use the standard deviation as a measure of uncertainty. The Poisson distribution is characterized by the property that its standard deviation equals the square root of the mean. Consequently, by considering this statistical behavior, one can compute the uncertainty in the event rate ratio as follows

$$\Delta q = \frac{1}{\sqrt{\text{Events}}} \tag{38}$$

The number of laser pulses fed to the detector does not have an uncertainty.

In the following table 3, one can now observe the results of the detected events at the SPAD corresponding to the respective transmission. These measurements were taken at both maximum and minimum gain settings, and the event rate ratio was determined. The event rate ratio q is equal to 1 when the same number of detections on the SPAD and a number of laser pulses occur. This was only achieved in the case of the maximum gain and a transmission rate of 15%, which, according to the table, would correspond to approximately $4,380$ signal photons per laser pulse. However, it is important to note that many of these events belong to the dark count and background radiation rates, which further increases the total number of events.

		@ min gain			**@ max gain**		
τ	$\Delta\tau$	**Events**	**q**	**Δq**	**Events**	**q**	**Δq**
0.00976	0.00011	84	0.00084	0.10911	431	0.00431	0.04817
0.01252	0.00013	149	0.00149	0.08192	751	0.00751	0.03649
0.01636	0.00014	307	0.00307	0.05707	1537	0.01537	0.02551
0.02152	0.00016	654	0.00654	0.03910	3063	0.03063	0.01807
0.02793	0.00018	1140	0.01140	0.02962	6457	0.06457	0.01244
0.03499	0.00022	2411	0.02411	0.02037	11324	0.11324	0.00939
0.0435	0.00024	4573	0.04573	0.01479	19851	0.19851	0.00709
0.05434	0.00027	8054	0.08054	0.01114	33911	0.33911	0.00543
0.06683	0.00031	15280	0.15280	0.00809	53890	0.53890	0.00431
0.08224	0.00035	24998	0.24998	0.00632	73951	0.73951	0.00368
0.09879	0.00039	39350	0.39350	0.00504	91108	0.91108	0.00331
0.1168	0.00043	57681	0.57681	0.00416	98836	0.98836	0.00318
0.1375	0.00047	80677	0.80677	0.00352	99981	0.99981	0.00316
0.15954	0.00051	91559	0.91559	0.00330	100171	1.00171	0.00316
0.18461	0.00055	98343	0.98343	0.00319	-	-	-
0.21224	0.00058	99862	0.99862	0.00316	-	-	-
0.24194	0.00062	99980	0.99980	0.00316	-	-	-
0.2724	0.00065	99985	0.99985	0.00316	101219	1.01219	0.00314

Tabelle 3: **The event rate ratio at minimum and maximum gain obtained at different transmission values.** The detected events on the SPAD are dependent on the transmission of attenuators. It is visible that the higher the transmission is, the more events are detected and the higher the calculated event rate ratio measured. The number of detected events at maximum gain is already five times higher starting from the highest attenuation, and it reaches a 100% event rate ratio at a transmission of 15%, whereas at the minimum gain setting, there is still only a 99% event rate at 27% transmission.

5.2.6 Calculating the Quantum Efficiency

After obtaining the photon count and the event rate ratio q one can calculate the quantum efficiency of the detector. Fig.31 and 30 illustrate q on the y-axis, while the x-axis represents the number of photons per pulse, with one set of data measured at the maximum gain setting and another at the minimum gain setting. The data points are represented by the green markers, while the blue curve represents a curve fitted to these data points using the equation

$$q = 1 - \exp\left(-N_{\text{photon}}\eta_{\text{QE}}\right) \tag{39}$$

from Eq.7, where the values for q and N were employed . Therefore, the quantum efficiency η_{QE} was the variable determined through the fitting process.

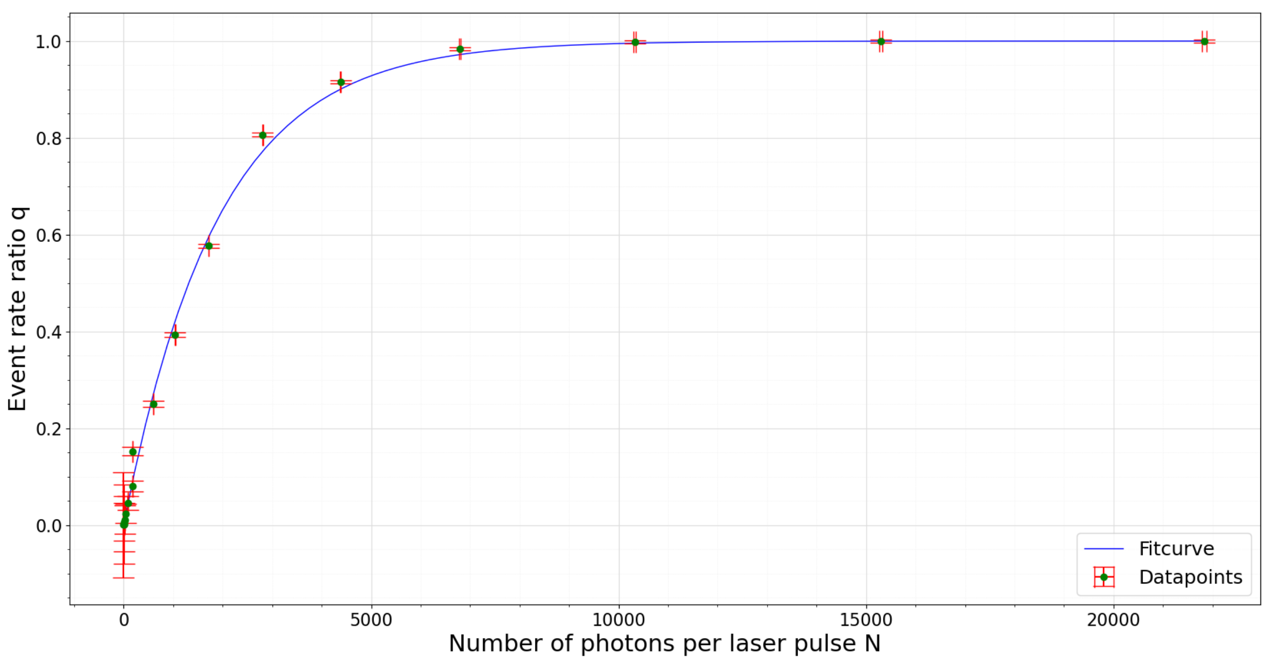

Abbildung 30: **Event rate ratio q against the number of photons per laser pulse N at the minimum gain setting.** The data points are represented in green, with their uncertainties in red and the curve fitted to the data points is in blue. A quantum efficiency η_{QE} of 0.05% is obtained by fitting the curve to the data points at minimum gain.

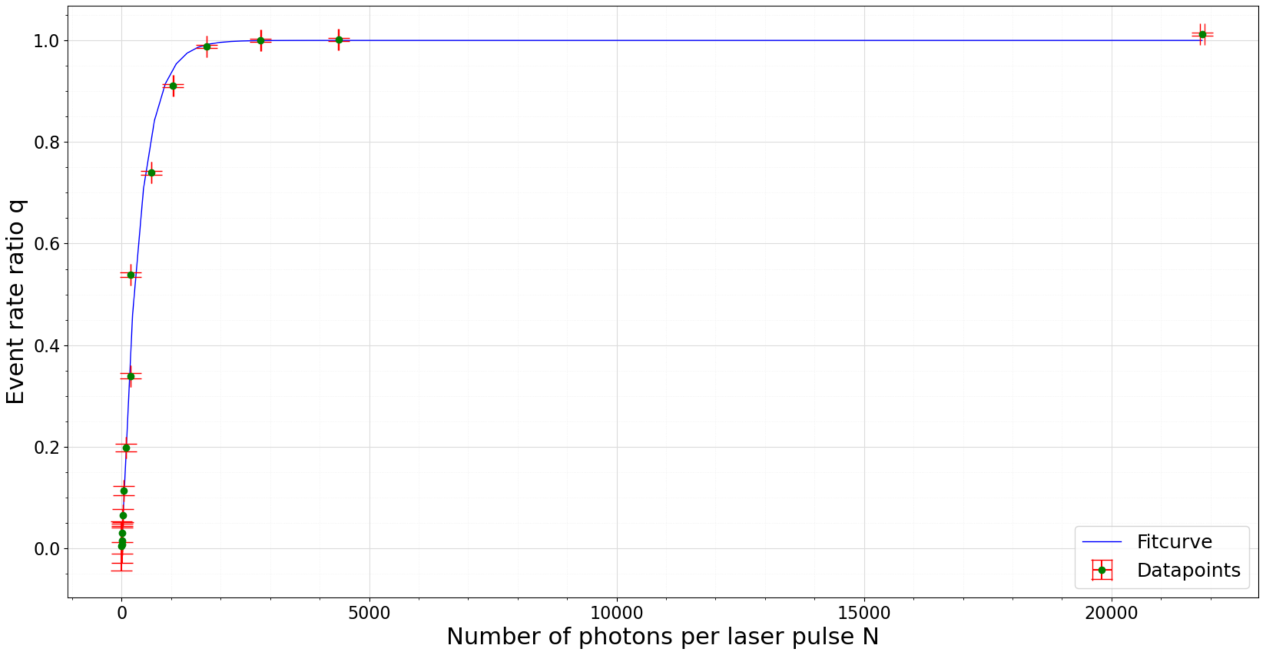

Abbildung 31: **Event rate ratio q against the number of photons per laser pulse N at maximum gain setting.** The data points are represented in green, the same as in Fig.30, with their uncertainties in red, and the curve fitted to the data points is in blue. A quantum efficiency η_{QE} of 0.3% is obtained by fitting the curve to the data points at maximum gain.

In Fig.31 below, one can observe that the curve quickly reaches an event rate ratio of 1 on the y-axis at an x-value of approximately 2500 photons per pulse, and then it remains steady. In contrast, in Fig.30, where the curve in Fig.31 has already reached the value of an event rate ratio of 1, the curve is still only at an event rate ratio of 0.8, and it does not approach the value 1 until around 10,000 photons per laser pulse. This already indicates that the quantum efficiency must be higher at maximum gain. By fitting the curve, the quantum efficiency was determined. It becomes evident that by minimizing the gain, one achieves a quantum efficiency of 0.05%, while at maximum gain, the quantum efficiency increases to 0.3%.

5.3 Laser Pulse Detection

The next step was to precisely detect the laser pulse in the measurements. The approach has evolved from random laser pulse direction onto the detector to conducting targeted measurements in realistic scenarios, emphasizing actual laser pulse detection. A dedicated light source was integrated into the setup behind the bandpass, simulating the natural background radiation. This background radiation varies depending on the albedo of the surface under consideration, such as dry earth or snow, and the telescope size, for instance, 10 cm or 30 cm. Fig.32 shows an illustration of the background radiation in outer space. The red elements represent these background photons, which must be considered when conducting experiments to ensure accurate results. This work mostly focuses on scenarios with an albedo of dry ground and a 10 cm wide telescope, because this scenario causes the fewest background photons.

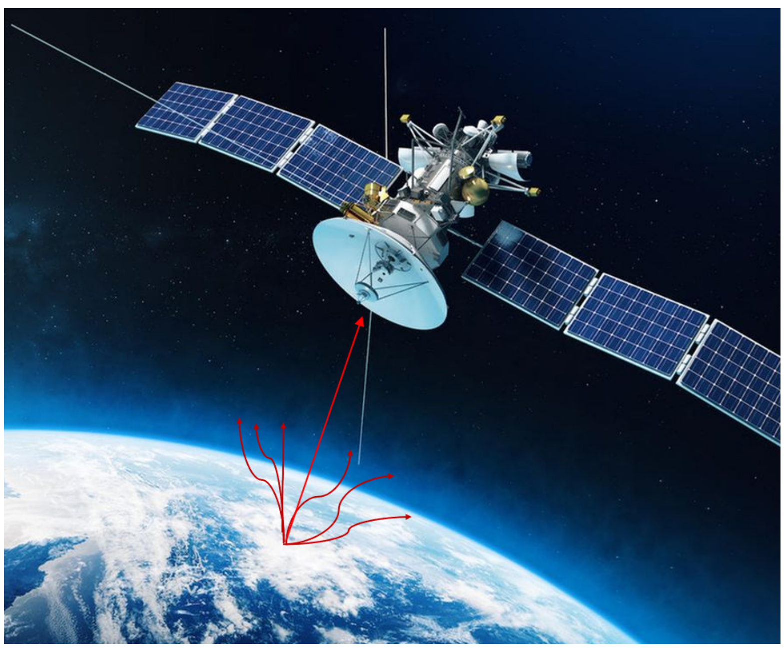

Abbildung 32: **Illustration of the natural background radiation in space.** In red, the background photons are shown, which need to be considered for adjustment to reality in the experiment. Depending on the surface being observed, the factor of background photons varies.

The light source was integrated into the setup before the detector, between the optical components. Two simulations were conducted in the experimental setup: The first scenario is an albedo for dry earth and a 10 cm telescope[1], which leads to 0.117 background photons per microsecond. In the second scenario with albedo as for snow and the same 10 cm telescope, 0.234 background photons per microsecond were observed.

These values have already been adjusted to the 1064 nm bandpass. More scenarios are shown in table 4. Albedo refers to the amount of sunlight or laser light reflected by the ground surface. Higher albedo values, such as in snowy conditions, lead to increased background photon rates. Reflection properties indicate how efficiently the ground or snow reflects incident light. Wavelength plays a crucial role, with shorter wavelengths like 532 nm being more affected by atmospheric scattering than longer wavelengths like 1064 nm. The size of the telescope also influences the detection rate, as larger telescopes capture more photons.

Scenario \ Wavelength	1064 nm	532 nm
Dry Ground + 10 cm telescope	0.117 /µs	1.68 /µs
Snow + 10 cm telescope	0.234 /µs	8.33 /µs
Dry Ground + 30 cm telescope	1.05 /µs	15.14 /µs
Snow + 30 cm telescope	2.1 /µs	47.97 /µs

Tabelle 4: **Detection rate of background photons per µs for various scenarios.** The detection rate depends on several factors, including the albedo, reflection properties, wavelength, and the size of the telescope.

When using a dry ground albedo and a 10 cm telescope, the least amount of background photons are present at a wavelength of 1064 nm. However, if the wavelength is changed to 532 nm, the number of background photons increases by a factor of 15. When using an albedo for snow and a 10 cm telescope at 1064 nm, the number of background photons doubles. The number of background photons is further increased by a factor of 8 when comparing a 10 cm telescope to a 30 cm telescope at 1064 nm. The highest level of background photons is observed when using a 30 cm telescope with a snow albedo at a wavelength of 532 nm.

Figure 33 below is a captured image of the oscilloscopes program. The x-axis represents time (in black) and the y-axis represents the voltage of the laser in blue and the voltage of the detector in red. What can be observed is in blue, the 2 ns wide laser diode current, and in red the detection of the SPAD, which is 15 ns wide due to the TTL signal of the SPAD. The dead time of 25 ns was added to the plot to display the time after which another event could be detected. The green shows the voltage of the variable optical attenuators.

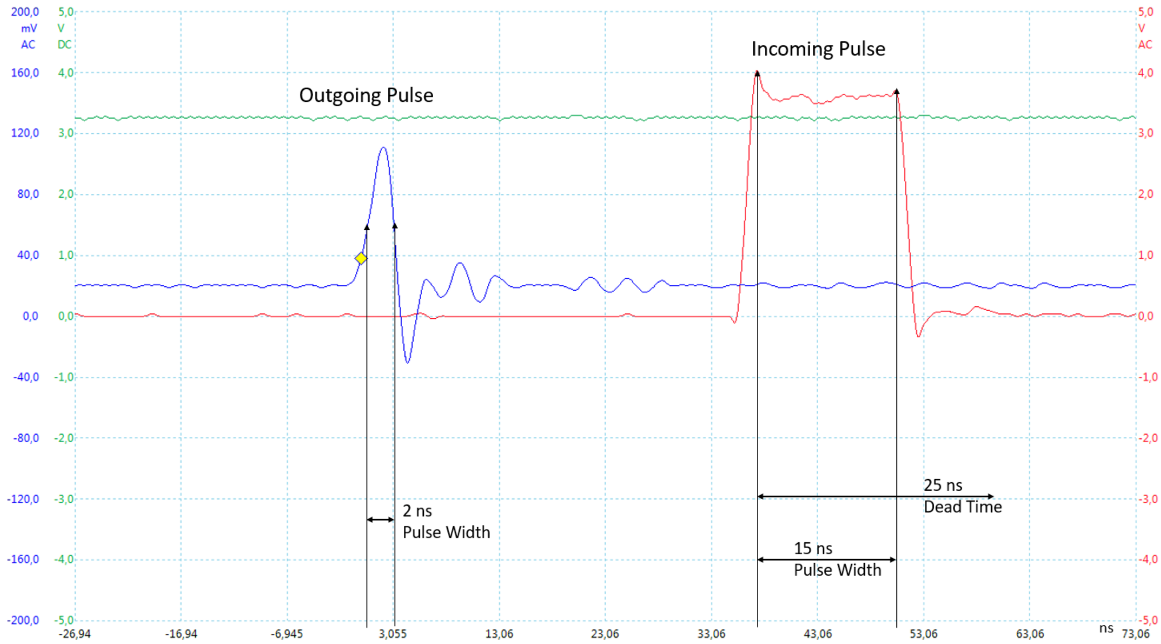

Abbildung 33: **Picture of the 2 ns wide pulse and detection by the SPAD in the PicoScope program.** In blue is the outgoing 2 ns wide pulse, and in red is the incoming pulse, detected by the SPAD. The 15 ns display the TTL signal of the detector, and the 25 ns display after which time another signal could be detected.

5.3.1 Measurements with Background Photons

The experiments in this thesis aimed to detect a single photon, so the transmission rate in the optical attenuators was increased slowly to minimize the number of photons per laser pulse. The generated laser pulse has a width of 2 ns. The measured voltages of the attenuators range from 3.2 V to 3.4 V, corresponding to transmission values ranging from 2.2% to 5.4%. The measurements conducted yielded a range of 10 photons up to about 170 photons per laser pulse.

Fig. 34 below illustrates multiple measurements, each consisting of a 25 μs range window, which is a predefined time interval used to assess data within it, equivalent to a distance of 3750 m. The x-axis represents the individual measurements and the y-axis the time. All points with the same x-value belong to the same measurement. Each point, when represented along the y-axis, corresponds to its respective time value. A total of 10,000 measurements were conducted, with a pre-trigger set to initiate the laser after 10 μs. Consequently, a laser pulse was directed to the detector precisely 10 μs into the measurement window. Each vertical column in the plot represents a measurement, wherein the laser was triggered once within the specified time interval. In Fig. 34, a distinct line becomes visible after 10 μs, indicating the detection of the laser pulse.

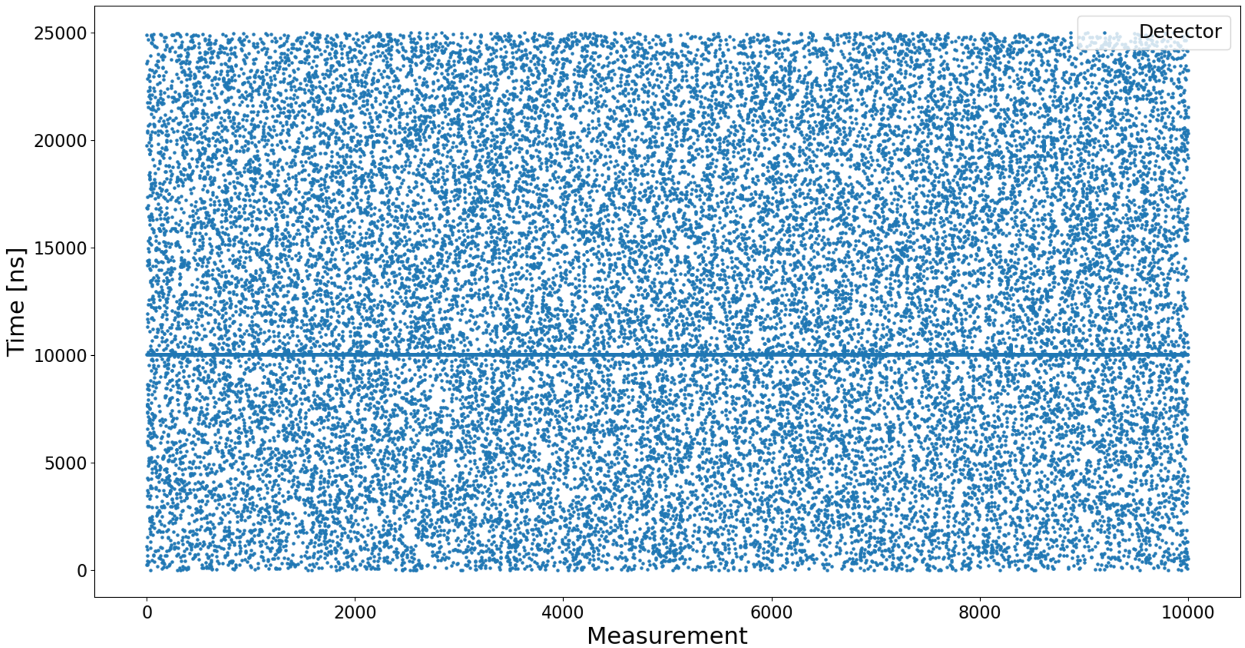

Abbildung 34: **Detection of laser pulses as a function of time for 10,000 measurements using a 2 ns wide laser pulse with an energy of 170 photons and an albedo for dry ground (0.117 background photons per μs).** Detected events as a function of time on the y-axis given for 10,000 measurements on the x-axis. Single measurements span a range of $25,000\,$ns, where the laser pulses are triggered at $10,000\,$ns. Each dot in the figure corresponds to one detection.

The line becomes more visible depending on the number of photons per laser pulse. Fig.35 below shows the same measurement as in Fig.34, but close up on 500 measurements. When now completing the same measurment, but with an energy of 10 photons instead 170 photons per laser pulse, by lowering the transmission of the attenuators, and an albedo for dry ground, one can see the results in Fig.36. Again it shows a close up on 500 measurements, and the line is very faint. In Fig.36 it is even less evident to distinguish between background photon events and laser pulse-induced events.

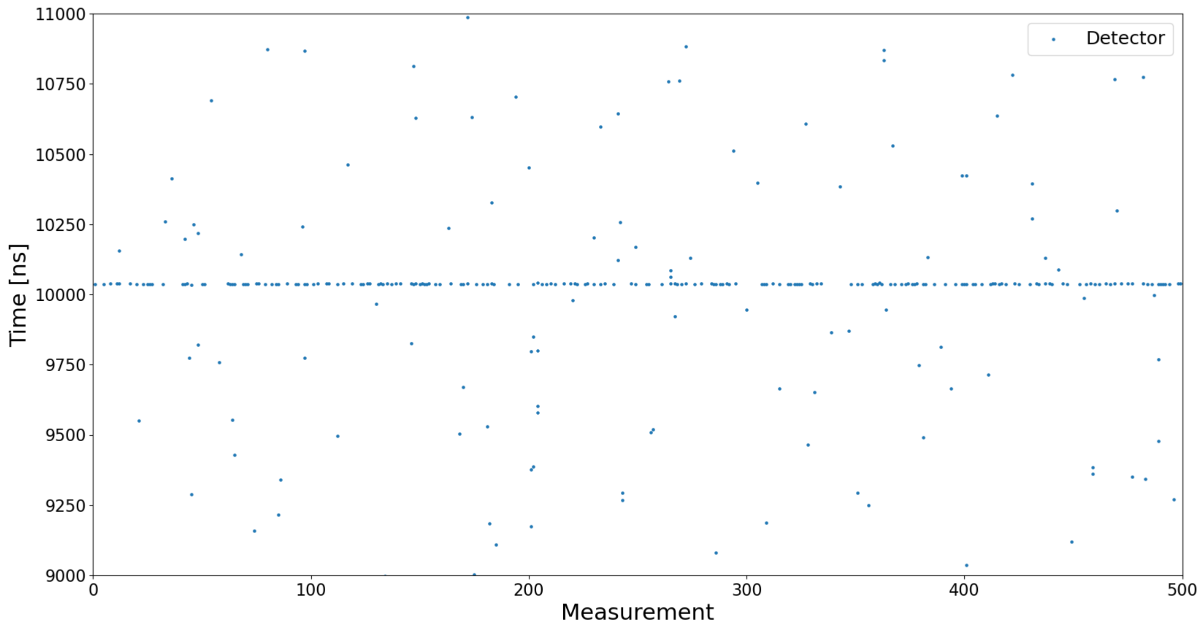

Abbildung 35: **Same as in Fig.34, but for only 500 measurements and using a laser energy corresponding to 170 photons per pulse and an albedo for dry ground.**

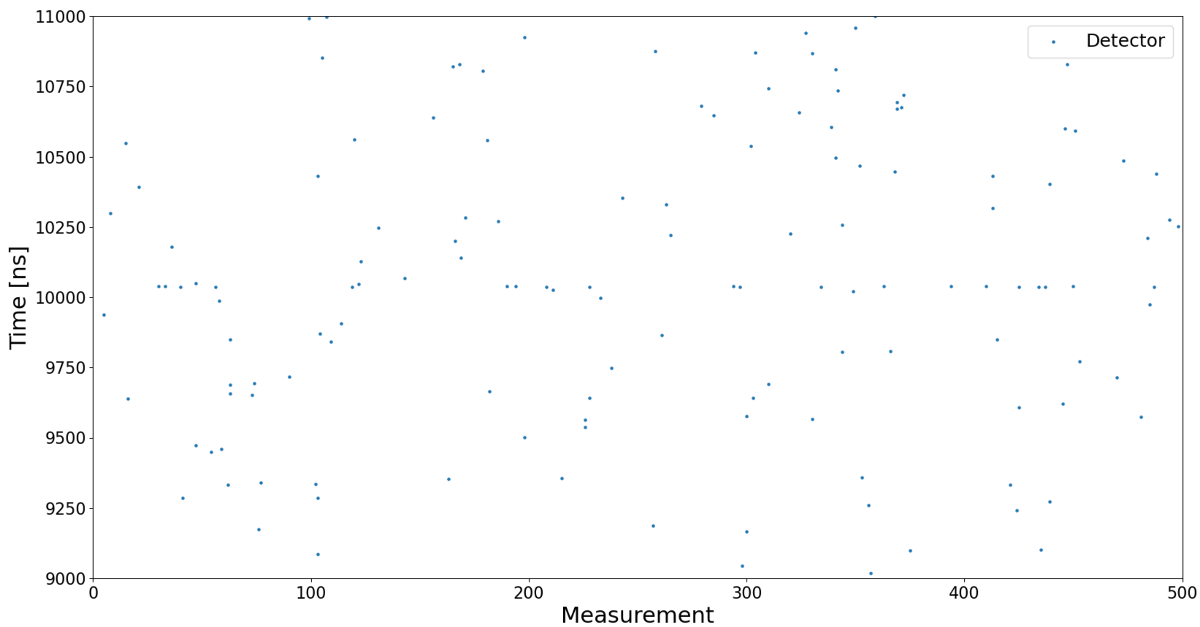

Abbildung 36: **Same as in Fig.34, but for only 500 measurements and using a laser energy corresponding to 10 photons per pulse and an albedo for dry ground.**

In Fig.37 below, 500 measurements are shown under the condition that the laser pulse is reflected on a snowy surface, leading to a higher background photon count. The laser energy was set to approximately 10 photons per pulse. The measurement range window was again fixed at 25 μs. Given a quantum efficiency of 0.3 %, the expectation would be to observe merely around 150 detected events out of 5000 laser pulses. Consequently, out of 500 measurements conducted, it is anticipated that only about 15 events would be observed due to the limited quantum efficiency of the detector. The presented Fig.37 illustrates the challenge of identifying the laser pulse.

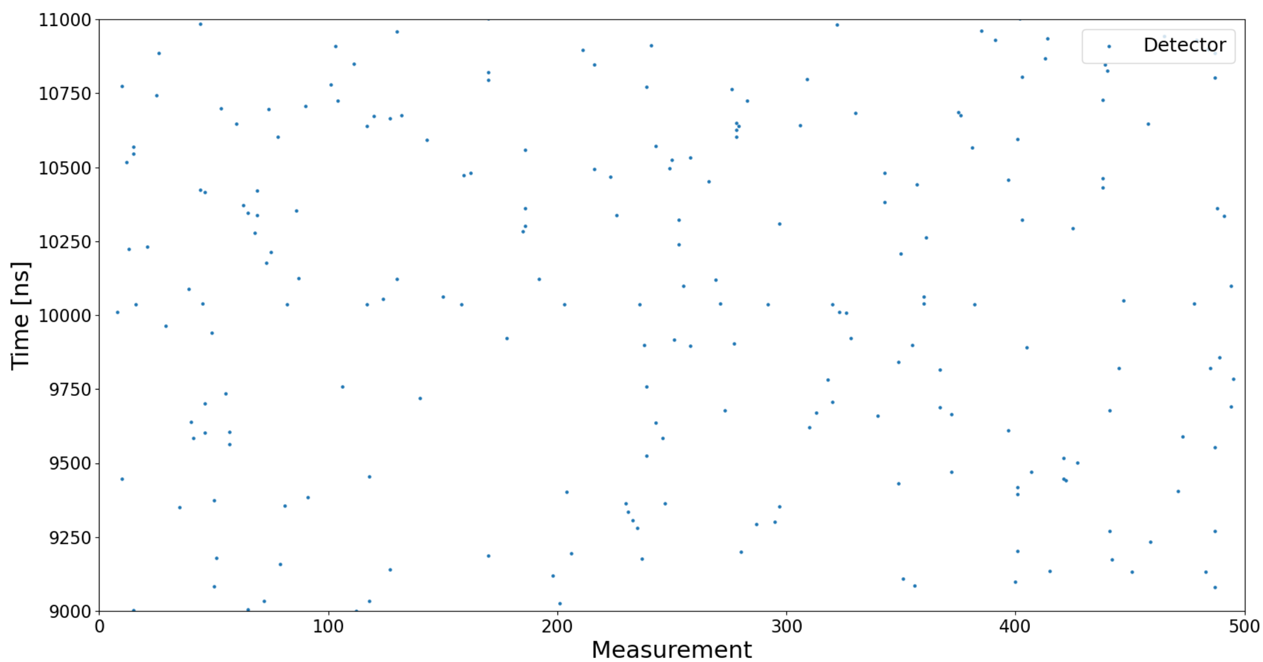

Abbildung 37: **Same as in Fig.34, but for only 500 measurements and using a laser energy corresponding to 10 photons per pulse and an albedo for snow.**

Upon closer inspection, some measurements exhibit multiple consecutive detector triggers, as illustrated in Fig.38. The red data points represent events triggered by the detector within a time window of 20 ns to 24 ns, which corresponds to the detector's dead time of 25 ns. This phenomenon is known as afterpulses, and it is caused by residual charges inside the photodiode after the quenching process. Afterpulses are additional or delayed signals recorded by the photodiode, often leading to inaccuracies in measurements.

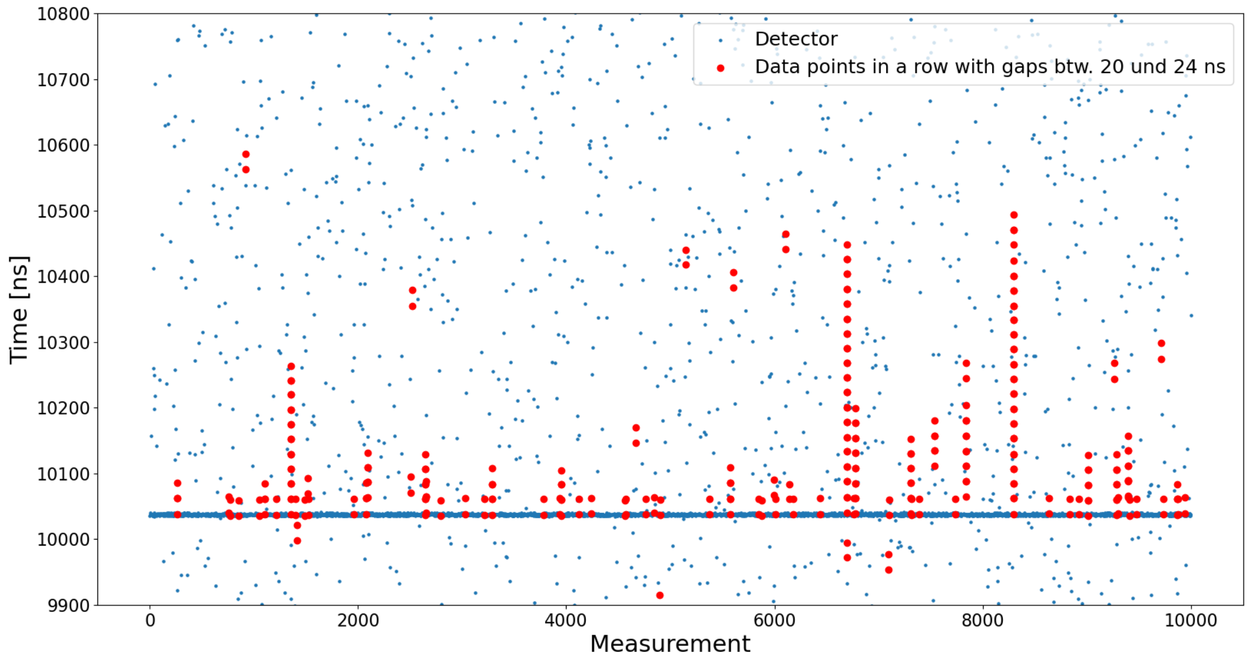

Abbildung 38: **Same as in Fig.34, using a laser energy corresponding to 170 photons per pulse and an albedo for dry ground, while illustrating the afterpulses of the detector, which are shown by the red dots.**

5.4 Pulse Identification

This chapter discusses how to detect the laser signal and distinguish it from background events. To achieve this, a 80 ns wide pulse was chosen, which would trigger three detections within that time frame, taking the detector's dead time into account. The 80 ns pulse was chosen for its flat and extended shape, in contrast to the 2 ns pulse previously used, while maintaining the same energy. This choice provides a more straightforward reference for comparing the measurements and also ensures consistency in laser energy, thereby maintaining the same number of photons per pulse. After the first triggering, the detector requires approximately 25 ns to recover, as illustrated in Fig.39. Three 15 ns long TTL signals and a total of 25 ns time windows could be detected in the 80 ns wide pulse. If successful, this approach would result in three or a maximum of four consecutive detections, leading to a detection of the laser pulse, distinguishable from random background events.

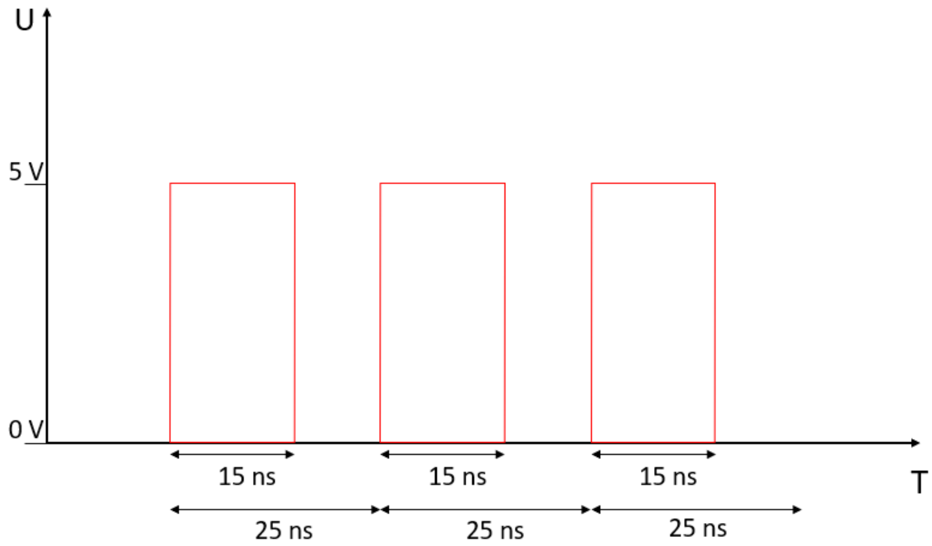

Abbildung 39: **TTL signal output of the detector as a function of time.** The illustration shows three 25 ns rage windows for an 80 ns wide pulse.

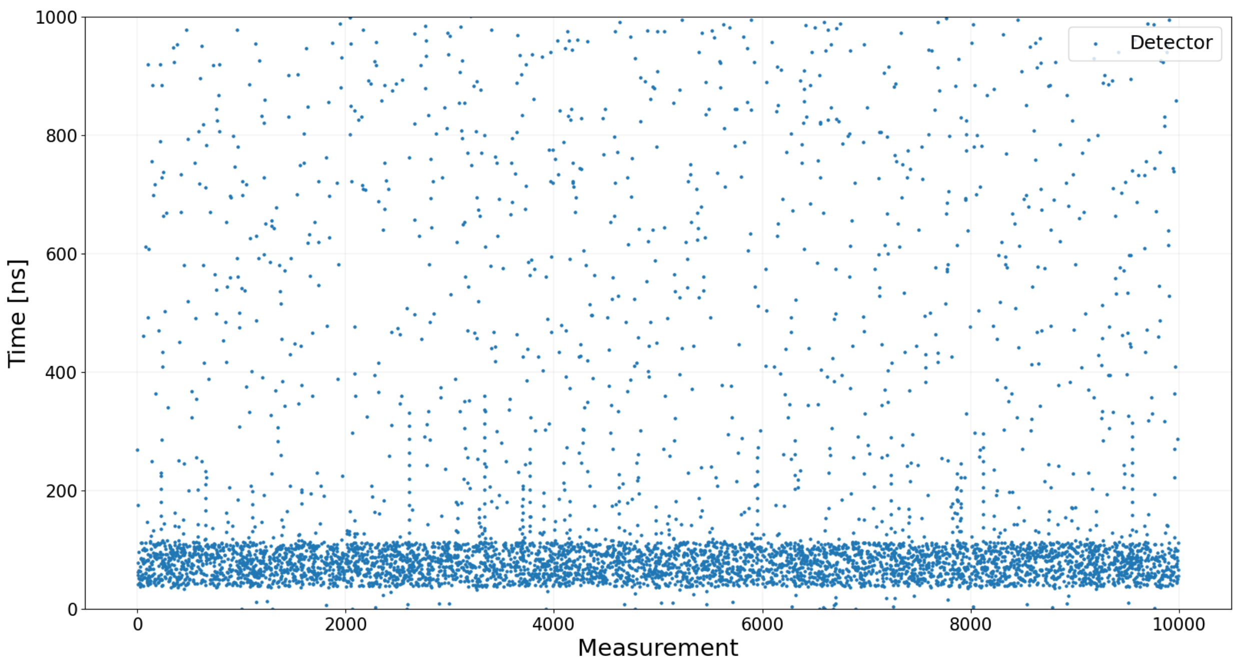

Abbildung 40: **Detection of laser pulses as a function of time for 10,000 measurements using a** 80 ns **wide laser pulse with an energy of 170 photons per pulse and an albedo for dry ground (0.117 background photons per** μ**s).** Detected events as a function of time on the y-axis given for 10,000 measurements on the x-axis. Single measurements span a range of 1,000 ns, where the laser pulses are triggered at 0 ns. Each dot in the figure corresponds to one detection.

Fig.40 above reveals 10,000 measurements, each lasting 25 μs, using approximately 170 photons per laser pulse. Again the x-axis represents the measurement and the y-axis the time. To enhance clarity, the plots were zoomed in to show data within a 1000 ns range on the y-axis. Notably, one can observe an 80 ns wide pulse, represented by the extended dark bar immediately following the laser pulse after about 30 ns, which corresponds to the time it takes for the laser pulse to travel through the optical chain. A close-up of the area of interest is shown in Fig.41. The detections within the 80 ns window still appear somewhat randomly distributed due to the low quantum efficiency of the employed detector, which means that the detector will not detect three signal photons per laser pulse with high certainty.

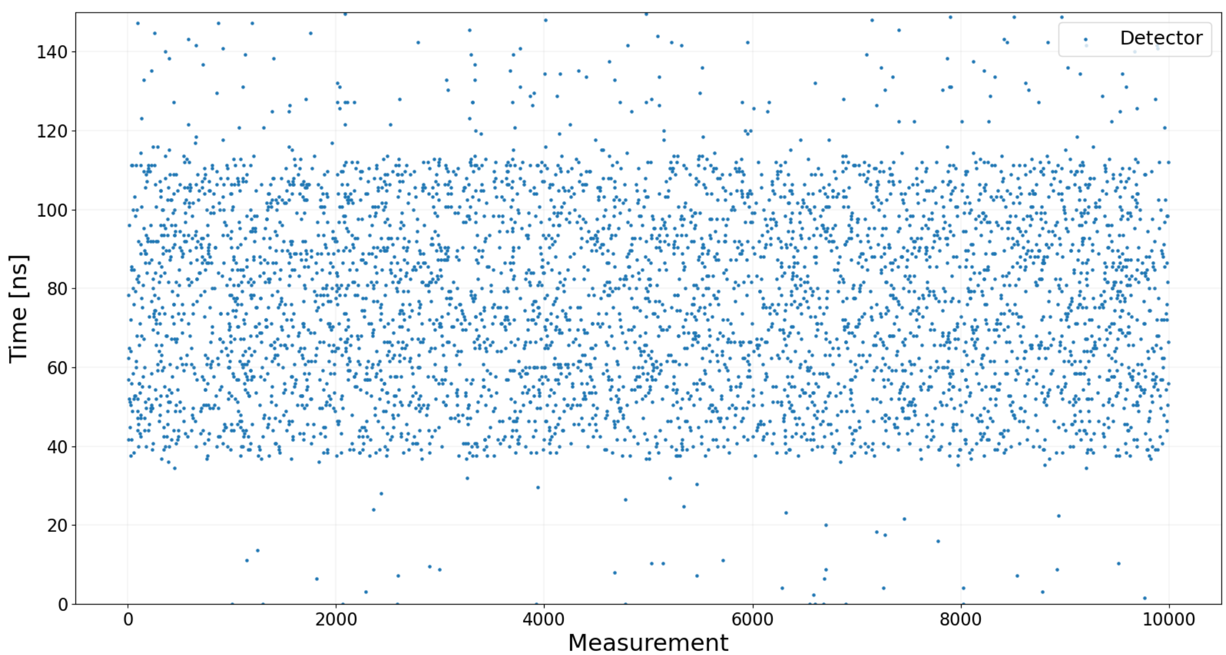

Abbildung 41: **Same as in Fig.40, but zoomed into the the time window of 140 ns.**

Fig.42 again shows 10,000 measurements each lasting 25 μs, but now the laser energy is only 10 photons per pulse. The dark bar is almost not visible anymore. Similarly, it is evident that when operating with 10 photons per laser pulse, very few detections are noticeable, and the transitions between the detection of the pulse and the detected background photons become considerably blurred.

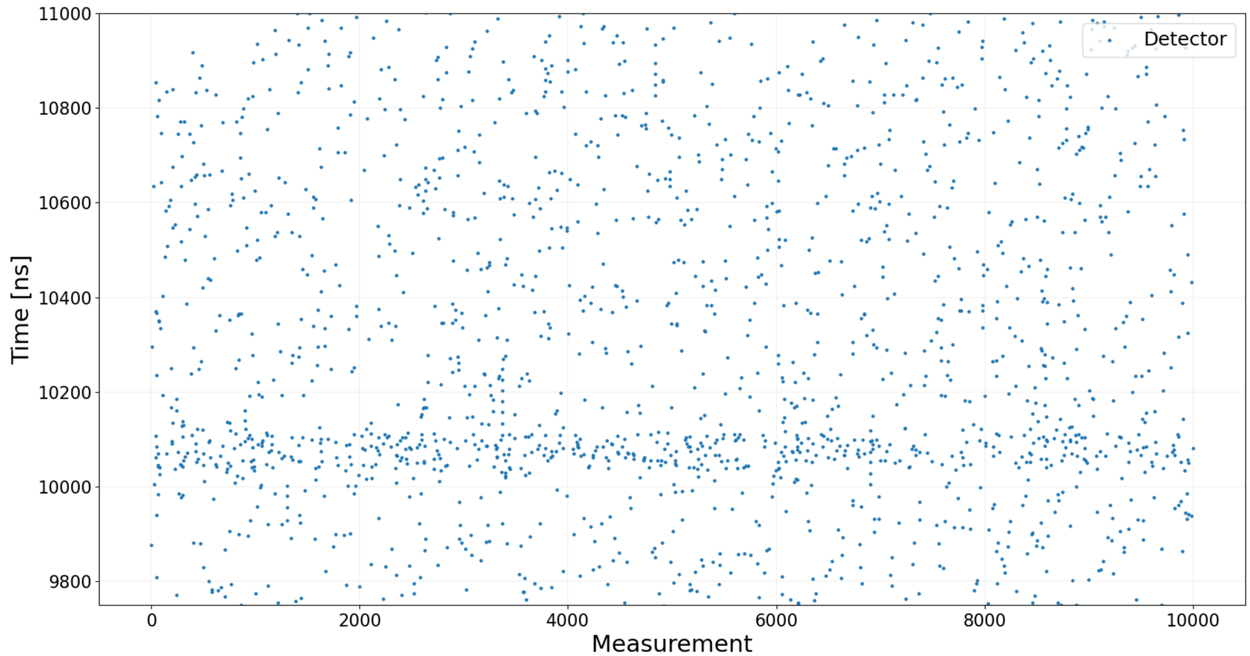

Abbildung 42: **Same as in Fig.40, the 80 ns pulse using a laser energy of 10 photons per pulse and an albedo for dry ground**

5.5 Five Signal Photons per Laser Pulse

The next step is to adjust the energy of the laser to a level where one can reliably detect five signal photons per laser pulse when considering the detector's quantum efficiency. Given a quantum efficiency of 0, 3%, one will now work with approximately 1700 photons per laser pulse, to reach 5 signal photons per pulse. To achieve the theoretically calculated number of 1700 photons per laser pulse, the following calculation is performed:

$$N_{\text{Background}} + N_{\text{Dark Count}} + (N_{\text{Measurements}} \times N_{\text{Photon}}) \times \eta_{\text{QE}}) \approx N_{\text{Events}} \tag{40}$$

$$15000 + 85 + ((5000 \times 1700) \times 0.003) \approx 40000 \tag{41}$$

The calculation aims to determine the number of detected events on the detector in 5000 measurements, when feeding the detector with 1700 photons per laser pulse, which, given a detector quantum efficiency of 0.3%, would correspond to 5 signal photons. The calculation incorporates the number of set background photons, which amounts to 0.117 photons per microsecond for an albedo of dry ground and a 10 cm telescope, roughly totaling 15000 photons across 5000 measurements over 25 μs each. In addition, there are dark counts, amounting to 85 counts when a dark event is detected every 1.48 ms. Finally, one must factor in the 1700 photons multiplied by 5000 measurements and the quantum efficiency. These combined factors result in approximately 40,000 events in 5,000 measurements, each with 1700 photons, yielding 5 signal photons.

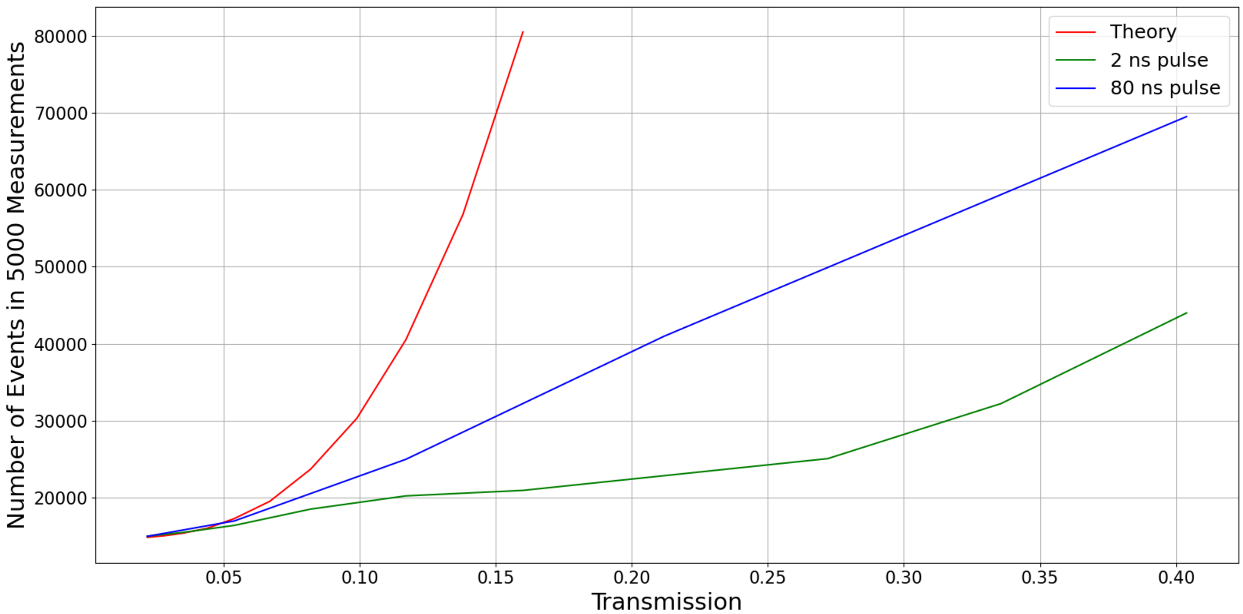

Abbildung 43: **Comparison of calculations and experiment.** Theoretically determined number of photons in 5000 measurements including background and dark count rate (red) as a function of attenuation with experimental results for the 2 ns (green) and 80 ns (blue) wide pulse.

When examining table 2, an expectation of around 1700 photons per laser pulse at a voltage of 3 V, so a transmission of 11.68% is apparent. However, it was necessary to increase the transmission for both laser pulses to achieve an amount of 1700 photons per pulse. This comparison is shown in Fig.43. The x-axis represents the transmission of the attenuators and the y-axis represents the number of events on the detector, when including the number of events per pulse in the 25 μs range window, the dark count rate and the number of background events. The red curve corresponds to the theoretically calculated values with Eq.41, by using the number of photons per pulse from table 2. In contrast, the blue and green curves represent the experimentally determined values of the 2 ns (green) and 80 ns (blue) wide laser pulse. All three curves only align up to a transmission of 5%. Above the theoretical curve exhibits a sharp increase. In contrast, the experimental curve for the 2 ns wide pulse continues to rise linearly and only slightly increases at around 27% transmission. In contrast, the 80 ns curve shows a slight increase starting at 12% transmission. These results demonstrate that in practice, the

80 ns wide pulse needs a lower transmission to achieve the same number of photons per pulse as the 2 ns wide pulse.

The discussion now focuses on the results of 10,000 measurements conducted within a 25 μs range window. Initially, the experiment employed a laser pulse with a duration of 2 ns, followed by one with a duration of 80 ns, both generating approximately 1700 photons per laser pulse. Due to the quantum efficiency of 0.3 %, a detection of around five signal photons per laser pulse is expected. The measurement can be conducted with the same energy for both pulses because the pulses are chosen in such a way that the 2 ns pulse has the same energy as the 80 ns; the 80 ns pulse is stretched out.

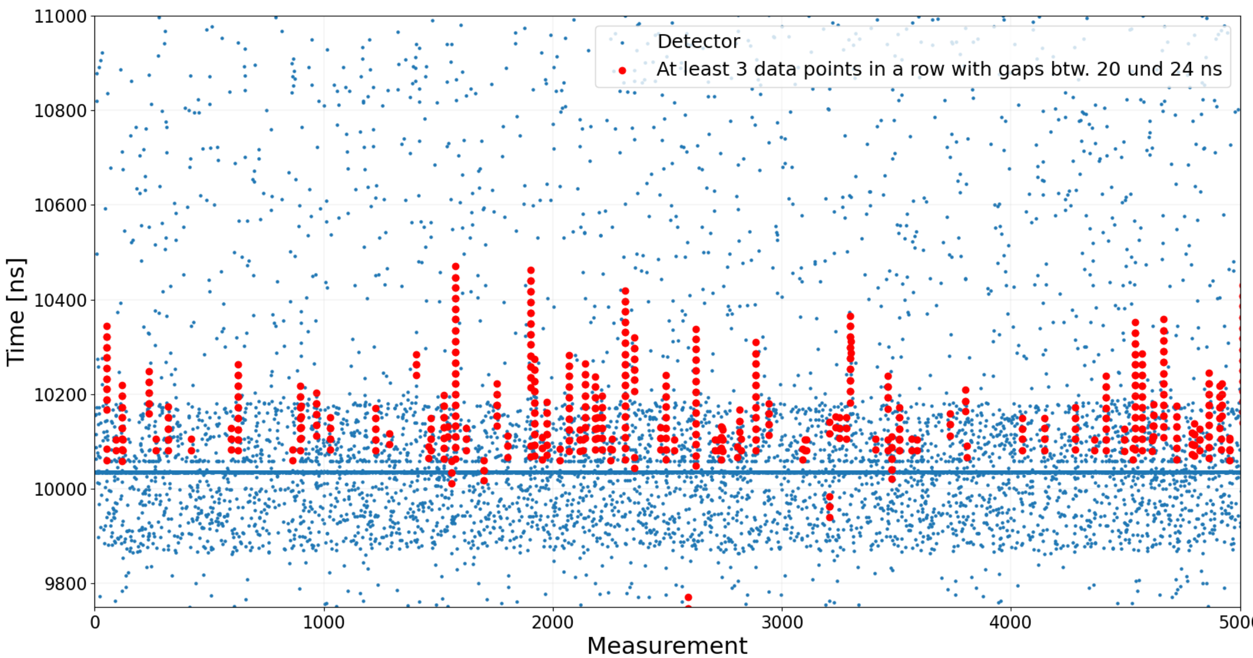

Abbildung 44: **Detection of laser pulses as a function of time for 5,000 measurements using a 2 ns wide laser pulse with an energy of 5 signal photons and an albedo for dry ground (0.117 background photons per μs).** Detected events as a function of time on the y-axis given for 10,000 measurements on the x-axis. Single measurements span a range of 1,200 ns, where the laser pulses are triggered at 10,000 ns. The red dots represent afterpulses.

In Fig.44 above, the results of the measurements are presented using a 2 ns wide laser pulse. These results reveal a consistent and continuous line pattern, strongly indicating successful laser pulse detection in nearly every measurement. Although, a distinct line becomes evident shortly after 10,000 ns following the laser activation through a pre-trigger, identifying the laser signal would remain challenging without knowledge of the laser trigger timing. Additionally, irregular afterpulses are also present, but can nevertheless be identified. Their quantity was estimated, revealing that they constitute approximately 20% of the total detected events.

The observed 300 ns wide band in the plots correspond to the plateau generated by the 2 ns laser pulse. Achieving such a short pulse requires raising the baseline potential of the laser very close to the emission threshold. This adjustment allows the laser current to increase rapidly, resulting in a strong, short pulse. Just before this stage, there is a continuous current flow referred to as continuous wave (CW) light.

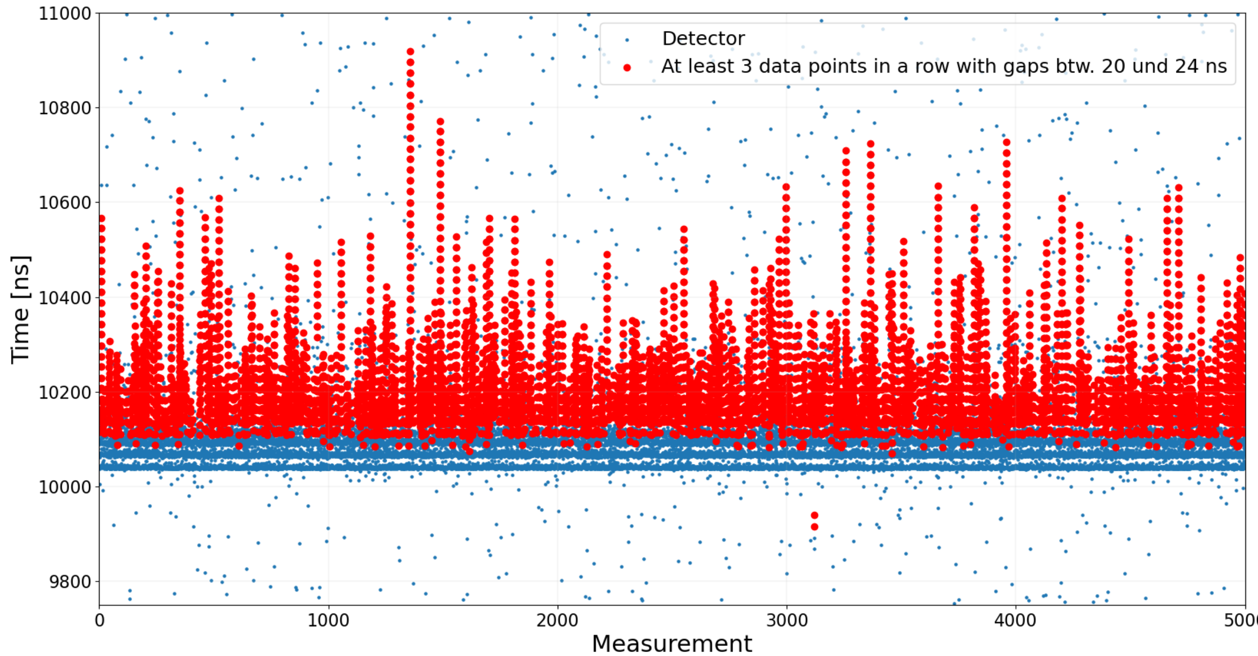

Abbildung 45: **Same as in Fig.44, but with an** 80 ns **wide laser pulse.** Single measurements span a range of 1,000 ns, where the laser pulses are triggered at 10,000 ns. The red dots represent afterpulses.

In Fig.45 above, the results of the measurements are presented using a 80 ns wide laser pulse with the same conditions as in Fig.44. In Fig.44 and Fig.45, afterpulses are also identifiable and are represented by the red points. These afterpulses were identified when at least three detections took place less than every 24 ns. The advantage of distinguishing the afterpulses from the three signal photons is that the signal photons consistently appear at intervals of at least 25 ns, the detector's dead time whereas the afterpulses do not adhere to this pattern, facilitating their distinction from the primary signal.

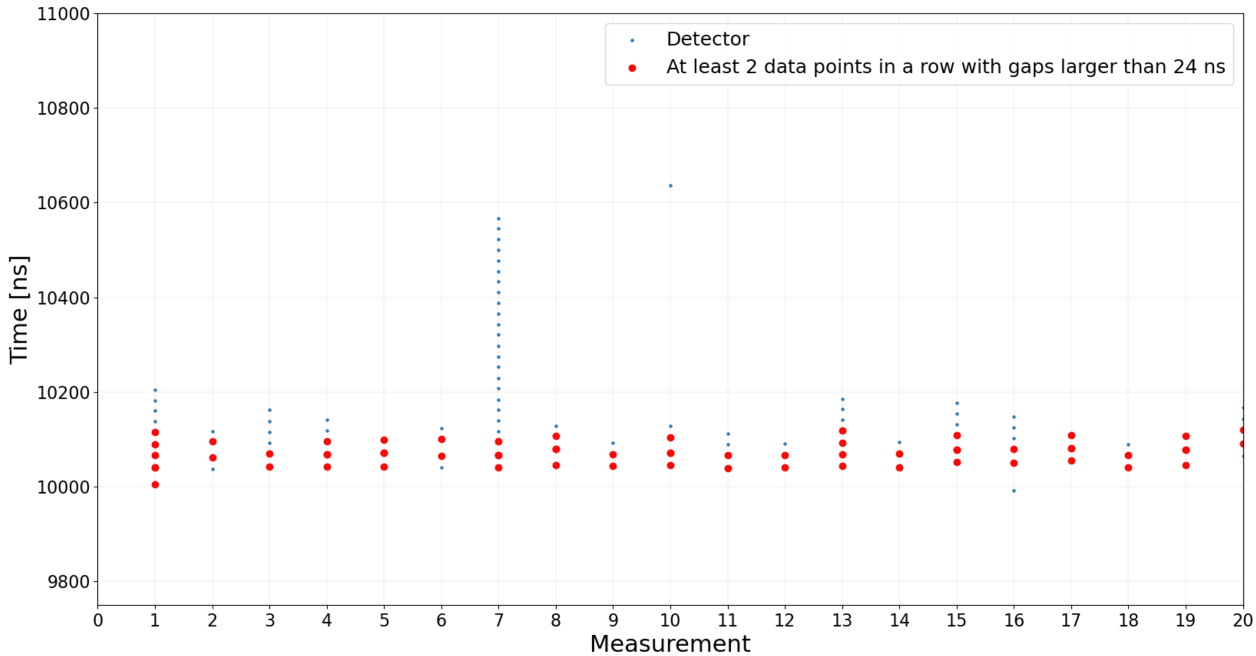

Abbildung 46: **Same as in Fig.45, but zoomed into the range window between 9800 ns and 1050 ns and only showing 20 measurements. The red dots represent data points with a gap larger than** 24 ns**.**

As is evident in Fig.45 and Fig.46, three-distinct and well-defined rows become apparent for the 80 ns pulse, indicating a successful detection. However, after these detections, a significant number of afterpulses emerge. As previously mentioned, afterpulses can be identified and isolated, effectively minimizing their influence on the measurements. However, it is important to note that the afterpulses can still distort the actual number of events detected. This becomes particularly relevant when one expects a certain number of events at the detector to yield a specific number of photons per pulse, which was done at the beginning of this chapter to obtain 5 signal photons per laser pulse. In such cases, it becomes necessary to consider a certain rate of afterpulses. In Fig.46 the red points illustrate the signal photons, by representing data points with a gap larger than 24 ns, another observation is that one constantly observes two to four consecutive detections occurring within a total interval of 80 ns as desired.

6 Discussion

The objective of this master thesis is to utilize a single photon avalanche Detector to reliably detect a laser pulse within a specific range window, using the least possible number of photons. To achieve this, an experimental setup was built in the laboratory, enabling the controlled emission of a given number of photons from a laser pulse. In this study, a series of measurements was conducted to comprehensively investigate various aspects of the detection system, including its sensitivity, accuracy, and efficiency, to optimize its performance for reliably detecting laser pulses with the minimum required number of photons.

To begin the measurements, the detector's dark count rate was established for the experimental setup. The Poisson method was utilized to analyze the detected events within a specific time interval. The results showed that at maximum gain, a dark count event took place on average every 1.48 ms. Subsequently, the photon counting efficiency of the detector was assessed by varying the attenuation of the beam and measuring the number of events at the detector. The results allowed for calculating the laser energy, photon count rate, and the detector's quantum efficiency, which was approximately 0.3 % at maximum gain and a wavelength of 1064 nm. Furthermore, the detection of laser pulses was explored under various background scenarios and the influence of afterpulses on the measurements was analyzed. Finally, a new laser pulse configuration was tested with the aim to reliably detect five pulses.

The laboratory setup employed a wavelength of 1064 nm for the laser pulse. This wavelength has been favored due to its availability and space heritage. It is the fundamental wavelength of the Nd:YAG laser, which is recognized for its robustness and space-tested characteristics. Using a frequency doubler, a wavelength of 532 nm could be generated.

6.1 Detector Characterization

In a Poisson process, events occur randomly and independently from each other with a constant average rate. The exponential Poisson distribution is the probability distribution that describes the time between events in a Poisson process. The detection mechanism of a Geiger mode APD depends on the generation of primary electrons and the subsequent current increase, which is a random process. Primary electrons can be created either by a dark current event inside the SPAD, a stray light photoelectron event, or an intended photon detection from a source such as a laser pulse.

The dark current event rate has been characterized in the chapter 5.1 and results are shown in Fig.26 and 27. As is evident in the figures, the average value of the dark current decreases for shorter tests due to the reduction in the measurement duration. The measurements taken over a period of 5 ms yielded an average rate of dark events every 1.2 ms. The longer and more frequent the measurements were taken, the more accurate the results became. For this reason, from that point onwards, the dark event rate of 1.48 ms was used for further calculations.

The tests of the laboratory setup were then conducted using a 25 μs range window, as this corresponds to a distance of 3750 m. In a 25 μs time window, a dark event occurs with a $\frac{1}{60}$ probability. This ratio makes the dark event rate irrelevant for the laboratory setup, as it does not affect the measurement principle.

The next step was a determination of the number of photons per laser pulse and calculating the detectors quantum efficiency. In table 3, the results of the detected events at the SPAD corresponding to the respective transmission are presented. The table's measurements cover the laser pulse transmission range, extending down to a transmission of only 0.9% of the laser pulse. Events were also detected at a lower transmission rate, however, an even lower transmission rate signifies less energy from the laser pulse, which resulted in an energy not even matching that of a single photon, which is not physically possible. This indicates that the events detected at lower transmission likely originate from the continuous-wave light of the laser or the dark event rate. At maximum gain, the measurements were only taken up to a transmission of 16%, with only one additional measurement at 27.7%, as the event rate was already quite high, which is not relevant for this study. What is evident is that at higher gain settings, the number of events increases rapidly. This aligns with the fact that gain enhances the detector's sensitivity.

To determine the detector's quantum efficiency, the event rate ratio q, arising from the ratio of the number of detected events on the detector to the number of pulses directed at the detector, was measured. Results are summarized in Fig.31 and 30, where the figures correspond to maximum gain and minimum gain. On the x-axis is the number of photons per pulse N and on the y-axis is the event rate ratio q. This means that when the event rate ratio q equals 1, the same number of events is detected as laser pulses are emitted. At maximum gain, approximately 2000 photons per laser pulse and at minimum gain around 10000 photons per laser pulse are needed to reach an event rate ratio of 100%. To put this into perspective: With maximum gain (quantum efficiency of (0.3%), 2000 photons equate to 6 signal photons per laser pulse.

Conversely, at minimum gain (quantum efficiency of (0.05%)), 10000 photons correspond to 5 signal photons per laser pulse. This difference that refers to the variation in the number of photons required to reach 5 or 6 signal photons stems from the sensitivity of the detector influenced by the gain. The substantial number of photons required to generate an event is already an indicator of the low quantum efficiency of the detector. In comparison to the detector manual [33], an efficiency of 5% was reported at a wavelength of 1064 nm and maximum gain. The quantum efficiency resulting from these investigations is over 16 times smaller than stated. The manufacturer's measurements, conducted with significantly broader bandwidth and a continuous wave source with very low sensitivity beyond 1000 nm, account for the observed discrepancy. Due to the even lower quantum efficiency at minimum gain, the investigations were exclusively conducted at maximum gain in this thesis.

6.2 Analysis of the Laser Pulse Identification

After determining the detector's dark count rate and quantum efficiency, the robustness of event detection within the recorded data was investigated. A continuous background radiation was integrated into the laboratory setup. As previously discussed, background radiation was estimated for various scenarios. The cases of background radiation included scenarios such as the reflection of sunshine on snow or dry ground using telescopes of sizes 10 cm or 30 cm. According to the SPADs manufacturer's specifications, the detector has a quantum efficiency of 50% at a wavelength of 532 nm. However, this would significantly increase the background count rate due to solar irradiation.

Table 4 represents a direct comparison of the background radiations, giving the detection of background photons per μs for various scenarios. What can be concluded from the table is that even when considering an albedo for a snow-covered surface using a 10 cm telescope, the background radiation increases by a factor of 36 when working with a wavelength of 532 nm instead of 1064 nm. In a 25 μs measurement window, one would detect over 200 background photons per measurement, compared to 5 photons at 1064 nm. The more background photons are detected, the more challenging it becomes to isolate the correct laser signal.

During the measurements, another phenomenon was noticed - the afterpulses. As explained in chapter 3.1.6, these appear at irregular intervals and are trapped photons that trigger repeated detections. These afterpulses consistently occur in sequences with intervals ranging from 20 ns to 24 ns and they manifest in groups of 2 to 10 consecutive events, making them distinguishable by filtering during data-processing.

Comparing the number of detected events against the theory, a strong alignment between theory and experiments is found. For example, a rough estimation would be to consider 5000 measurements in the scenario of background radiation corresponding to sunlight reflection from dry ground and a 10 cm telescope. The laser emits 5000 pulses, with each pulse generating approximately 170 photons on average, totaling around 850,000 photons. Due to the quantum efficiency of 0.3% this results in approximately 2550 detected events. In the background noise, an average of 585 background photons per microsecond will be recorded over 5000 measurements. This leads to a total of 14625 events when this count is converted into a 25 μs time window. The dark event occurs every 1.48 ms, equivalent to approximately 85 events. In total, this amounts to around 12,000 events in 5000 measurements. When compared to experimental results, there is a good alignment within the measurement errors.

6.3 New Method for Identifying the Laser Pulse

A method known as temporal filtering was employed to detect and distinguish the laser signals. For this purpose, a 80 ns long laser pulse was generated in the setup. During the time period in which the laser is emitted, the detector is expected to detect three or a maximum of four signals due to its dead time. Therefore, the laser energy was set to correspond to 1700 photons per pulse. Considering the quantum efficiency of 0.3%, this translates to only five signal photons per pulse.

As discussed in chapter 5.5 in Fig.43, the 80 ns wide pulse needed a lower transmission to achieve the same number of photons per pulse as the 2 ns wide pulse. The reason for this is the occurrence of afterpulses, which occur much more frequently during the 80 ns wide pulse compared to the 2 ns. This results in a faster increase in the number of detections than with the 2 ns pulse. A summary of the number of photons per laser pulse is seen in table 2. The increasing rate of background events, afterpulses, and the detector dead time are not included in the calculations. The values provided in table 2 accurately represent the number of photons per laser pulse for low transmission settings. However, as the transmission increases beyond a certain point, these values deviate from the ideal scenario. This deviation is primarily due to the fact that the ideal curve used for calculations does not account for factors such as the increasing rate of background events, the more frequent occurrence of afterpulses during the 80 ns wide pulse compared to the 2 ns pulse, and the presence of the detector's dead time. These additional factors become increasingly influential as the transmission level rises, leading to a departure from the idealized calculations and a more complex relationship between transmission and the number of photons per laser pulse.

Through closer observations of the CW and background light detections in the measurements, it was noticed that the number of photons increases significantly when the transmission rises over an amount of 5% transmission in the attenuators. This leads to a higher count of dark counts, and additionally, as the dark counts increase, they also start triggering afterpulses. This results in a less precise number of clicks on the detector.

Upon closer examination of the measurements, a phenomenon associated with transmission levels was observed. Specifically, when the transmission exceeds 5% within the attenuators, there is a notable increase in the detected photon count. This increase in photon count, because of the higher transmission rate, is linked to a higher frequency of dark counts. Additionally, the increased dark counts trigger afterpulses in the detector, which introduces variability in the accuracy of our event counts. In essence, the findings reveal a non-linear relationship between transmission, dark counts, and afterpulse generation.

In summary, the investigation initially assumed the detection of five photons per laser pulse based on the number of detected events. However, it was observed that reducing the attenuator settings led to an increase in background photons and afterpulses, particularly with the 80 ns pulse. After the laser pulse is emitted, it takes approximately 35 ns for the light to travel through the optical chain to reach the detector. By analyzing the initial 80 ns following the emission of the laser pulse, which occurs approximately 35 ns after the pulse is generated, it was evident that 100% of the events during this timeframe were laser signals, indicating the presence of enough photons per laser pulse.

To provide a meaningful perspective, it's important to note that while one cannot precisely determine the number of photons per pulse, the experimental setup in this thesis operated at an energy of approximately 10^{-16} Joules per laser pulse, which is approximately 12 to 13 orders of magnitude smaller than what is required for APDs. It stands in high contrast to projects employing avalanche photodiodes, such as BE-LA [1], where laser pulses are operated with 50 mJ, or projects like ATLAS [2], where pulse energies reach as high as 660 mJ. This underscores the exceptional sensitivity and precision achieved within the experimental setup employing single photon avalanche detectors even at energy levels significantly lower than those in comparable projects.

As a result, the exact number of signal photons per laser pulse, was affected by noise and background interference. The aim was to be able to detect three events, even in the presence of noise and afterpulsing. With this setup, it was possible since one can directly detect three events that are staggered in time right after the signal is emitted. Sometimes there may be only two events, but most of the time, three distinct and sometimes even four events occur within the 80 ns window. This ensures accurate pulse timing determination.

6.4 Outlook

Identifying quantum efficiency and dead time as fundamental parameters represents significant progress by this research. These findings are relevant for understanding and optimizing SPADs. Future investigations will explore the use of alternative detectors to enhance these parameters further.

Additionally, it is essential to consider another critical parameter for precise time-of-flight measurements: Timing jitter, the temporal discrepancy in photon detection, which plays an essential role in the performance of SPADs[26]. It can impact the accuracy of time-of-flight measurements, especially when looking at greater distances. Recent progress in manufacturing and materials technology offers avenues for improving SPAD detector performance, notably in reducing timing jitter. As an example, well-developed SPAD devices have been manufactured using cutting-edge 40 nm Si technology, resulting in impressively low timing jitter of just 170 ps[16]. To put this into perspective, the light in the experimental setup in this thesis needs 35 ns to go through the optical chain, which is 170,000 times longer than the timing jitter of the SPAD device.

Furthermore, considering the findings of the experiments of this thesis, it seems worthwhile to explore the possibility of conducting a statistical analysis on the number of detections within the 80 ns timeframe. This analysis could provide insights into the detection characteristics and patterns. Understanding whether there are typically 2, 3, or 4 detections within this timeframe can contribute to a deeper comprehension of the experimental results and help optimize the detector parameters for future measurements. This statistical approach may contribute to the refinement of data post-processing techniques.

The detector used in this laboratory setup had a QE of 0.3% and an afterpulsing probability exceeding 20%. Additionally, it had an active area of over 500 μs. A smaller active area results in a faster response time. Detectors with sub-ns dead times already exist [22], promising a detector dead time of only 0.9 ns and an afterpulsing probability of just 0.14%. However, these detectors operate at a wavelength of 490 nm. The experiments deliberately did not consider this wavelength range due to the increased background count rate. Regarding the use of detectors with sub-nanosecond dead times and a wavelength of 490 nm, suitable laser sources are available for such applications. Some common types of lasers in this wavelength range include diode lasers, solid-state lasers, and lasers generated by frequency-doubling green laser light at 532 nm [23], such as the Protera 532. In addition to the previously mentioned laser sources, semiconductor laser diodes have been developed that directly emit coherent light at 490 nm [6]. These diodes use advanced wide-band-gap semiconductors known as II-VI materials, particularly ZnSe-based (Zinc Selenide) single-quantum-layer structures. These materials are the components that enable these diodes to emit light directly at the desired 490 nm wavelength. These lasers can help increase the response time of the detectors and reduce the probability of afterpulsing.

When attempting to minimize the probability of afterpulses and the dead time of the detector, a balance must be struck. The challenge arises because the detector is often placed in a non-responsive state due to reduced afterpulses, which extends the dead time. However, if a more sensitive detector is used to minimize the dead time, there is more afterpulsing[22]. Further investigations seem advisable on whether afterpulses can be effectively eliminated during data post-processing, through dedicated software or algorithms.

7 Conclusion

In this master's thesis, a comprehensive investigation into single-photon detection technology and its applicability in laser altimetry for planetary research was conducted. The objective was to develop and evaluate an experimental laboratory setup capable of reliably detecting laser pulses with the minimal required number of photons, thereby advancing the precision and efficiency of altimetry measurements.

The study characterizes the SPAD employed in the laboratory setup. Parameters such as quantum efficiency and dark count rate were measured and analyzed. The quantum efficiency, which quantifies the detector's ability to capture photons from laser pulses, was approximately 0.3% at maximum gain. Meanwhile, the dark count rate, signifying detection events without incident light, was determined to occur every 1.48 ms. These characterizations formed the foundation for subsequent experiments.

Laser pulses with varying pulse shapes were generated to simulate realistic altimetry scenarios, and their interaction with the SPAD was examined. Special attention was given to detecting laser signals within a specified time window, distinguishing laser events from background noise and afterpulses. A method termed temporal filtering was introduced, utilizing an 80 ns laser pulse to facilitate the accurate identification of laser signals within a short timeframe. This approach allowed for the detection of three distinct laser events, thus enhancing the precision of pulse timing determination.

Moreover, the study delved into the impact of factors like transmission settings, background radiation, and afterpulsing on the efficiency of laser pulse detection. The results revealed a non-linear relationship between transmission, dark counts, and afterpulse generation. As the transmission of the attenuators increased, so did the photon count, leading to a more pronounced influence of dark counts and afterpulsing, affecting the accuracy of event counts.

A notable observation was the remarkable sensitivity of the experimental setup, which operated at energy levels on the order of 10^{-16} J per laser pulse. This distinction underscores single-photon avalanche detectors' exceptional precision and sensitivity, even at significantly lower energies.

In conclusion, this thesis provides insights into the behavior and performance of single-photon detectors and demonstrates their potential to advance laser altimetry in planetary research. By addressing noise, background radiation, and afterpulsing challenges, this work contributes to the refinement of altimetry techniques. This research aims to contribute to improving the accuracy and sensitivity of altimetry measurements for planetary surfaces and environments.

Literatur

[1] Christoph Becker. Systemauslegung eines single photon detection laser altimeters für eine kleinsatellitenmission im leo, 2023.

[2] Jack L Bufton. Laser altimetry measurements from aircraft and spacecraft. *Proceedings of the IEEE*, 77(3):463–477, 1989.

[3] Ghioni M. Lacaita A. Samori C. Zappa F. Cova, S. Avalanche photodiodes and quenching circuits for single-photon detection. applied optics.

[4] Daniel G Fouche. Detection and false-alarm probabilities for laser radars that use geiger-mode detectors. *Applied optics*, 42(27):5388–5398, 2003.

[5] Fabrizio Guerrieri, Simone Tisa, Alberto Tosi, and Franco Zappa. Two-dimensional spad imaging camera for photon counting. *IEEE Photonics Journal*, 2(5):759–774, 2010.

[6] Michael A Haase, J Qiu, James M DePuydt, and H Cheng. Blue-green laser diodes. *Applied Physics Letters*, 59(11):1272–1274, 1991.

[7] Eugene Hecht. *Optik*. Walter de Gruyter GmbH & Co KG, 2023.

[8] Hauke Hussmann, Kay Lingenauber, Reinald Kallenbach, Keigo Enya, Nicolas Thomas, Luisa M Lara, Christian Althaus, Hiroshi Araki, Thomas Behnke, Jose M Castro-Marin, et al. The ganymede laser altimeter (gala): key objectives, instrument design, and performance. *CEAS space journal*, 11:381–390, 2019.

[9] J. Binger J. Bartholomäus Chr. Hüttig S. Meiré Chr. Becker S. Reinert P. Werner M. Grott H. Hussmann K. Lingenauber, Chr. Althaus. Miniaturized laser altimeter for small satellite applications (in review). 2023.

[10] Fritz Kurt Kneubühl and Markus Werner Sigrist. *Laser*. Springer-Verlag, 2008.

[11] Hermann Kolanoski and Norbert Wermes. *Teilchendetektoren*. Springer, 2016.

[12] M López, A Meda, G Porrovecchio, RA Starkwood, M Genovese, G Brida, M Šmid, CJ Chunnilall, IP Degiovanni, and S Kück. A study to develop a robust method for measuring the detection efficiency of free-running ingaas/inp single-photon detectors. *EPJ Quantum Technology*, 7(1):14, 2020.

[13] Eamonn M Murphy, Nicola Rando, Peter Falkner, and Anthony Peacock. Lape: laser altimeter for planetary exploration. In *Laser Radar Technology for Remote Sensing*, volume 5240, pages 10–16. SPIE, 2004.

[14] Thomas A Neumann, Anthony J Martino, Thorsten Markus, Sungkoo Bae, Megan R Bock, Anita C Brenner, Kelly M Brunt, John Cavanaugh, Stanley T Fernandes, David W Hancock, et al. The ice, cloud, and land elevation satellite–2 mission: A global geolocated photon product derived from the advanced topographic laser altimeter system. *Remote sensing of environment*, 233:111325, 2019.

[15] Lucio Pancheri, Nicola Massari, Fausto Borghetti, and David Stoppa. A 32x32 spad pixel array with nanosecond gating and analog readout. In *International Image Sensor Workshop (IISW)*, pages 8–11, 2011.

[16] S Pellegrini, B Rae, A Pingault, D Golanski, S Jouan, C Lapeyre, and B Mamdy. Industrialised spad in 40 nm technology. In *2017 IEEE International Electron Devices Meeting (IEDM)*, pages 16–5. IEEE, 2017.

[17] Axcel Photonics. Product specifications 1064nm single-mode 14-pin butterfly module laser diodes.

[18] Physics and Radio Electronics. Photodiode, 2015.

[19] Simina Aurelia Rebegea. Nanosecond laser ablation of thin film material libraries, 2018.

[20] Dieter Renker. Geiger-mode avalanche photodiodes, history, properties and problems. *Nuclear Instruments and Methods in Physics Research Section A: Accelerators, Spectrometers, Detectors and Associated Equipment*, 567(1):48–56, 2006.

[21] Bahaa EA Saleh and Malvin Carl Teich. *Grundlagen der Photonik*. John Wiley & Sons, 2008.

[22] Fabio Severini, Iris Cusini, Davide Berretta, Klaus Pasquinelli, Alfonso Incoronato, and Federica Villa. Spad pixel with sub-ns dead-time for high-count rate applications. *IEEE Journal of Selected Topics in Quantum Electronics*, 28(2: Optical Detectors):1–8, 2022.

[23] Andrei V Shchegrov, Arvydas Umbrasas, Jason P Watson, Dicky Lee, Charles A Amsden, Wonill Ha, Glen P Carey, Vincent V Doan, Bryan Moran, Alan Lewis, et al. 532-nm laser sources based on intracavity frequency doubling of extended-cavity surface-emitting diode lasers. In *Solid State Lasers XIII: Technology and Devices*, volume 5332, pages 151–156. SPIE, 2004.

[24] Markus Werner Sigrist. *Laser: Theorie, Typen und Anwendungen*. Springer, 2018.

[25] David E Smith, Maria T Zuber, Glenn B Jackson, John F Cavanaugh, Gregory A Neumann, Haris Riris, Xiaoli Sun, Ronald S Zellar, Craig Coltharp, Joseph Connelly, et al. The lunar orbiter laser altimeter investigation on the lunar reconnaissance orbiter mission. *Space science reviews*, 150:209–241, 2010.

[26] Feiyang Sun, Yue Xu, Zhong Wu, and Jun Zhang. A simple analytic modeling method for spad timing jitter prediction. *IEEE Journal of the Electron Devices Society*, 7:261–267, 2019.

[27] Orazio Svelto, David C Hanna, et al. *Principles of lasers*, volume 1. Springer, 2010.

[28] Nicolas Thomas, Hauke Hussmann, and Luisa M Lara. The bepicolombo laser altimeter (bela): a post-launch summary. *CEAS space journal*, 11:371–380, 2019.

[29] Robin N Thor, Reinald Kallenbach, Ulrich R Christensen, Philipp Gläser, Alexander Stark, Gregor Steinbrügge, and Jürgen Oberst. Determination of the lunar body tide from global laser altimetry data. *Journal of Geodesy*, 95(1):4, 2021.

[30] Thorlabs. Air-spaced doublet collimators: Fc/apc, fc/pc, sma.

[31] Thorlabs. Electronic variable optical attenuators, voltage controlled sm fiber coupled.

[32] Thorlabs. Hard-coated uv/vis/nir bandpass filters.

[33] Thorlabs. Spdma manuel.

[34] Thorlabs. Ø1n-bk7 best form spherical lenses, ar coating: 1050-1700 nm.

[35] Binhao Wang and Jifang Mu. High-speed si-ge avalanche photodiodes. *PhotoniX*, 3(1):1–22, 2022.

[36] Hui Zhou, Yuwei Chen, Juha Hyyppä, and Song Li. An overview of the laser ranging method of space laser altimeter. *Infrared Physics & Technology*, 86:147–158, 2017.

Selbstständigkeitserklärung

Ich erkläre hiermit, dass ich die vorliegende Arbeit selbstständig verfasst und noch nicht für andere Prüfungen eingereicht habe. Sämtliche Quellen einschließlich Internetquellen, die unverändert oder abgewandelt wiedergegeben werden, insbesondere Quellen für Texte, Grafiken, Tabellen und Bilder, sind als solche kenntlich gemacht. Mir ist bekannt, dass bei Verstößen gegen diese Grundsätze ein Verfahren wegen Täuschungsversuchs bzw. Täuschung eingeleitet wird.

Berlin, 02.10.2023

S. Meiré